SPE 109749

A New Inversion Method To Interpret Flow Profiles From Distributed Temperature and Pressure Measurements in Horizontal Wells

K. Yoshioka, D. Zhu, and A. D. Hill, Texas A&M University

This paper was prepared for presentation at the 2007 SPE Annual Technical Conference and Exhibition held in Anaheim, California, U.S.A., 11–14 November 2007.

Abstract

The increasing deployment of distributed temperature and pressure measuring devices in intelligent well completions is providing the means to monitor the inflow profiles of wells without any well intervention. If the profiles of pressure and/or temperature are affected by the inflow profiles of the various phases being produced, it is possible to estimate these flow profiles by inverting the measured temperature and pressure profiles. This inversion process is particularly challenging for horizontal wells because the pressure drop along the well is usually small, and temperature changes, caused primarily by Joule-Thomson effects, are also small.

This paper presents an inversion method that interprets distributed temperature and pressure data to obtain flow rate profiles along horizontal wells. The inversion method, which is based on the Levenberg-Marquardt algorithm, is applied to minimize the differences between the measured profiles and the profiles calculated from a forward model of the well and reservoir flow system.

We present synthetic and field examples in this paper to illustrate how to use the inversion model to interpret the flow profile of a horizontal well. The synthetic examples show that even with single-phase oil production, the inflow profile can be estimated in many cases with the inversion method developed. The method is even more robust when water or gas is produced along discrete intervals in an oil production well because of the unique temperature signature of water or gas production. We applied the inversion method to temperature and pressure profiles measured with production logs in a North Sea horizontal oil producing well. The method successfully inverted pressure and temperature profiles and the profiles of oil and water flow rates determined compared well with the flowmeter derived profiles.

Introduction

In the past decades, thousands of wells have been drilled horizontally and in multiple directions to obtain larger contact volume with the reservoir. Because of the growing complexities of the recent well trajectories, running conventional production monitoring tools on appropriate locations has become difficult and costly. Flow rate, pressure, and temperature are the principle parameters we wish to measure through production logging. For the pressure and temperature measurements, continuous profiles of these in a complex well can be obtained accurately and inexpensively due to the advanced technology of fiber optics. Since the first fiber optic sensor was implemented in a well in Shell's Sleen Field in 1993[1], the use of distributed temperature sensors (DTS) and distributed pressure sensors (DPS) has become increasingly common for monitoring producing sections of horizontal wells[2-4].

As for the flow rate measurement, metering flow rate is still difficult especially under the multiphase flow conditions that occur in most wells. For multi-phase flowing wells, despite the recent advancements in technologies and equipments, a comprehensive solution to measuring flow rates and holdups of the phases is evasive[5]. However, to take full advantages of intelligent wells, which can control inflow capacities from different producing sections without interventions, real-time monitoring of the downhole flow conditions such as flow rate profiles and locations of excessive water or gas influx is essential. Therefore, to realize the value of intelligent wells, downhole flow conditions are either measured or translated from measurable parameters (e.g. density, pressure, and/or temperature) in horizontal, multi-lateral, or multi-branching wells. Some interpretation studies have shown how production profiles can be obtained by matching such data[6,7].

This research proposes an inversion method to obtain downhole inflow conditions from temperature and pressure profile data. We set the parameters to be estimated as productivities or inflow rates of each segment. From continuous temperature and pressure data along the well, we invert them into the desired inflow rates by applying the Levenberg-Marquardt algorithm[8].

Forward Model

The forward model predicts flow rate and profiles of pressure and temperature. The prediction model presented previously[9]

is used as a forward model in this study. It considers a rectangular reservoir whose top and bottom boundaries are sealed (no flow boudary) and which has constant fluxes at the both sides, and also assumes steady-state segregated flow in the reservoir. The physical description of the forward model is shown in Fig. 1.

The forward model couples reservoir flow and wellbore flow and solves both equations simultaneously. The temperature behavior in the reservoir is governed by[10]

$$\rho C_p \mathbf{u}\cdot\nabla T - \beta T\mathbf{u}\cdot\nabla p - K_T\nabla^2 T + \mathbf{u}\cdot\nabla p = 0. \qquad (1)$$

Eq. 1 can be solved analytically in 1D along streamlines in the reservoir. Examples of the reservoir temperature profiles are depicted in Fig. 2 and properties used for the examples are listed in Table 1. Temperature behaviors are compared under the same boundary temperatures (180 ^{o}F) and pressure drawdowns (300 psi) in the reservoir. Primary temperature changes are caused by Joule-Thomson effect and differences in Joule-Thomson coefficients create inflow temperature (temperature at the well) differences.

Pressure and temperature profiles of wells are obtained by coupling with the wellbore model that accounts for heat and mass transfer to or from the formation. We show wellbore temperature and flow rate profiles for a water entry case (Fig. 3) and gas entry case (Fig. 4). The well with large diameter listed in Table 2 is used for this example. Both temperature profiles show an anomalous temperature drop where water or gas entry happens. The temperature drops can be understood by looking at the differences in the inflow temperatures in Fig. 2. The Joule-Thomson effect of water is not as large as that of oil. Thus, a water entry appears as wellbore temperature cooling on the profile. A gas entry also reduces the wellbore temperature, with its effect often being cooling which goes below the geothermal temperature. Thus, we observe a more intense temperature drop on the profile.

As shown in the examples, the locations of water or gas entry can be found from the temperature profiles. For a detailed study about water or gas entry detection, see Yoshioka *et al.*[11] In the following synthetic inversion examples, we give locations of water or gas entry as prior knowledge to the inversion problems; the inflow rates of the phases are determined by the inversion procedure.

Inversion Method

We regard the total well flow rate and the pressure and temperature profiles as observation data, and productivity (inflow) distribution as parameters to be estimated. The relationships between the productivity profile and the resulting temperature and pressure profiles are highly nonlinear.

Let the relationship between parameter vector $\mathbf{w}$ and the forward model-generated observations be represented by $f(\mathbf{x};\mathbf{w})$. $f(\mathbf{x};\mathbf{w})$ is a function of both observation space $\mathbf{x}$ and parameter $\mathbf{w}$, and maps N-dimensional parameter space into M-dimensional observation space. Given observations, $\mathbf{y}$, we define an objective function as a squared error between the model generated predictions and the observations as

$$E(\mathbf{w}) = \left\| \left(f(\mathbf{x};\mathbf{w}) - \mathbf{y} \right) \right\|^2. \qquad (2)$$

The objective function is minimized by applying the Levenberg-Marquardt method whose upgrade vector is given by

$$\mathbf{w} = \mathbf{w}_0 - \left(\mathbf{H} + \lambda\mathbf{I}\right)^{-1}\mathbf{d}, \qquad (3)$$

where $\mathbf{w}_0$ and I are the current parameter vector and identity matrix respctively, and λ is called Marquardt parameter. The letters $\mathbf{d}$ and $\mathbf{H}$ stand for the derivative and the Hessian respectively. They are given by the following equations:

$$\mathbf{d} = \mathbf{J}^T\left(f(\mathbf{x};\mathbf{w}_0) - \mathbf{y}\right), \qquad (4)$$

and

$$\mathbf{H} = \mathbf{J}^T\mathbf{J}, \qquad (5)$$

where $\mathbf{J}$ is a Jacobian matrix given by

$$\mathbf{J} = \nabla f(\mathbf{x};\mathbf{w}_0). \qquad (6)$$

while $\mathbf{d}$ is the actual derivative of $E(\mathbf{w})$, $\mathbf{H}$ is the approximate Hessian obtained by neglecting the second order derivative.

Application

We now apply a Levenberg-Marquardt method to our problem, which has flow rate, temperature, and pressure data as observations. Supposing downhole pressure and temperature profiles are measured at N points, we will obtain N points of pressure and temperature, respectively, in addition to the total well flow rates of each phase.

We denote the measured pressure data as

$$\mathbf{p}_m = \left[p_{m1}, p_{m2}, \cdots, p_{mN}\right]^{\mathrm{T}}, \qquad (7)$$

and the temperature measurements as

$$\mathbf{T}_m = \left[T_{m1}, T_{m2}, \cdots, T_{mN}\right]^{\mathrm{T}}. \qquad (8)$$

The total well flow rates of each phase (1 = oil, 2 = water, and 3 = gas) are

$$\mathbf{q}_m = \left[q_{m1}, q_{m2}, q_{m3}\right]^{\mathrm{T}}. \qquad (9)$$

The parameters we wish to estimate from these data are the productivity profile along the well, which, for the rectangular reservoir, is proportional to the average permeability of each segment. Following the notation of the previous section, the parameters can be written as

$$\begin{aligned}\mathbf{w} &= \left[k(x_1), k(x_2), \cdots, k(x_N)\right]^{\mathrm{T}} \\ &= \left[k_1, k_2, \cdots, k_N\right]^{\mathrm{T}}\end{aligned}. \qquad (10)$$

From the forward model with N segments, we can calculate N pressures and N temperatures respectively. The calculated pressure profile from the model is

$$\mathbf{p}_c(\mathbf{w}) = \left[p_{c1}, p_{c2}, \cdots, p_{cN}\right]^{\mathrm{T}}, \qquad (11)$$

and temperature profile is

$$\mathbf{T}_c(\mathbf{w}) = [T_{c1}, T_{c2}, \cdots, T_{cN}]^{\mathrm{T}} . \quad (12)$$

Additionally we have production of each phase in each segment

$$\mathbf{q}_c(\mathbf{w}) = [q_{c1}, q_{c2}, q_{c3}]^{\mathrm{T}} , \quad (13)$$

where subscript c stands for calculated.

Now we define the objective function as a squared difference of the model-calculated values and measurements. However, we cannot treat temperature, pressure, and flow rate equally because they have different impacts on the productivity profile. Thus, we need to weigh each measurement in defining the error term. Hence, we define the error components as follows

$$\mathbf{e}_p = \mathbf{D}_p{}^{1/2}(\mathbf{p}_c - \mathbf{p}_m), \quad (14)$$

$$\mathbf{e}_T = \mathbf{D}_T{}^{1/2}(\mathbf{T}_c - \mathbf{T}_m), \quad (15)$$

and

$$\mathbf{e}_q = \mathbf{D}_q{}^{1/2}(\mathbf{q}_c - \mathbf{q}_m). \quad (16)$$

where $\mathbf{D}_p$, $\mathbf{D}_T$, and $\mathbf{D}_q$ are weights for each error element and are diagonal matrices. See Appendix A for how to scale these weights. Then we can define the objective function as

$$\begin{aligned} E(\mathbf{w}) &= \mathbf{e}_p{}^{\mathrm{T}}\mathbf{e}_p + \mathbf{e}_T{}^{\mathrm{T}}\mathbf{e}_T + \mathbf{e}_q{}^{\mathrm{T}}\mathbf{e}_q \\ &= \sum_{j=1}^{N}\left[(\mathbf{D}_p)_{jj}(p_{cj} - p_{mj})^2 + (\mathbf{D}_T)_{jj}(T_{cj} - T_{mj})^2\right] , \\ &\quad + \sum_{i=1}^{3}(\mathbf{D}_q)_{ii}(q_{ci} - q_{mi})^2 \end{aligned} \quad (17)$$

where the Jacobian matrices $\mathbf{J}_p$, $\mathbf{J}_T$, and $\mathbf{J}_q$ are given by

$$(\mathbf{J}_p)_{jk} = \frac{\partial e_{pj}}{\partial k_k} = \left(\mathbf{D}_p{}^{1/2}\right)_{jj}\frac{\partial p_{cj}}{\partial k_k}, \quad (18)$$

$$(\mathbf{J}_T)_{jk} = \frac{\partial e_{Tj}}{\partial k_k} = \left(\mathbf{D}_T{}^{1/2}\right)_{jj}\frac{\partial T_{cj}}{\partial k_k}, \quad (19)$$

and

$$(\mathbf{J}_q)_{ik} = \frac{\partial e_{qi}}{\partial k_k} = \left(\mathbf{D}_p{}^{1/2}\right)_{ii}\frac{\partial q_{ci}}{\partial k_k}. \quad (20)$$

Therefore, the kth component of the derivative vector $\mathbf{d}$ is given as

$$\begin{aligned} d_k &= \left(\mathbf{J}_p{}^{\mathrm{T}}\mathbf{e}_p\right)_k + \left(\mathbf{J}_T{}^{\mathrm{T}}\mathbf{e}_T\right)_k + \left(\mathbf{J}_q{}^{\mathrm{T}}\mathbf{e}_q\right)_k \\ &= \sum_{j=1}^{N}\left[(\mathbf{D}_p)_{jj}(p_{cj} - p_{mj})\frac{\partial p_{cj}}{\partial k_k} + (\mathbf{D}_T)_{jj}(T_{cj} - T_{mj})\frac{\partial T_{cj}}{\partial k_k}\right] \\ &\quad + \sum_{i=1}^{3}\left[(\mathbf{D}_q)_{ii}(q_{ci} - q_{mi})\frac{\partial q_{ci}}{\partial k_k}\right] \end{aligned} \quad (21)$$

Similarly, the Hessian matrix H is

$$\mathbf{H} = \mathbf{J}_p{}^{\mathrm{T}}\mathbf{J}_p + \mathbf{J}_T{}^{\mathrm{T}}\mathbf{J}_T + \mathbf{J}_q{}^{\mathrm{T}}\mathbf{J}_q . \quad (22)$$

The component of the matrix is estimated as

$$\begin{aligned} (\mathbf{H})_{jk} &= \sum_{l=1}^{N}\left[(\mathbf{D}_p)_{ll}\frac{\partial p_{cl}}{\partial k_j}\frac{\partial p_{cl}}{\partial k_k} + (\mathbf{D}_T)_{ll}\frac{\partial T_{cl}}{\partial k_j}\frac{\partial T_{cl}}{\partial k_k}\right] \\ &\quad + \sum_{i=1}^{3}\left[(\mathbf{D}_q)_{ii}\frac{\partial q_{ci}}{\partial k_j}\frac{\partial q_{ci}}{\partial k_k}\right] \end{aligned} . \quad (23)$$

Each component of the Jacobian matrices can be obtained numerically. For instance, $\partial p_{cj}/\partial k_k$, can be computed by perturbing p_{cj} while keeping other parameters constant. The sensitivity of p_{cj} to k_k is approximated as

$$\frac{\partial p_{cj}}{\partial k_k} \cong \frac{p_{cj}(k_1, \cdots, k_k + \delta k, \cdots k_N) - p_{cj}(k_1, \cdots, k_k, \cdots k_N)}{\delta k} . \quad (24)$$

As seen from Eq. 24, calculating a sensitivity of one parameter k_k requires at least one forward model run. Therefore, to compute the whole Jacobian matrix, we need to generate *N* forward runs. Starting from an initial guess of the parameters, $\mathbf{w}_0$, the update rule follows Eq. 3. The schematic of the inversion process is shown in Fig. 5.

Synthetic and Field Examples

With the inversion method described above, we show synthetic and field examples in this section. Synthetic examples include single-phase oil and gas examples, and detections of water and gas entry. In the field example, we use production log data measured from a horizontal well in the North Sea which is producing oil and water.

As input parameters we give to the inversion program, we can think of some combinations such as pressure and temperature profiles or temperature and temperature derivative. To determine which combination of the observations provides the best outcome, we have examined and compared the parameter estimation results using synthetic reservoir productivity profiles in Appendix B. From the numerical experiments, we choose pressure and temperature profiles in addition to total production rate of each phase as the observed data.

"Observations" are generated from a forward model following the "true" permeability distribution that we set up, and then inversion of the true permeability distribution is performed by matching the observations that are generated from the model. The measurement resolutions of the pressure, temperature and flow rate are assumed to be on the order of 0.1 psi, 0.01 ^{o}F, and 1 b/d respectively. The measurements are logged over 20 points located every 100 ft along the well.

Single-phase oil production. We show inversion results of the permeability distributions of cases A and B shown in Fig. 6a for single-phase oil production. With the large diameter well described in Table 2 with a bottomhole pressure of 3900 psi, the generated observations of pressure and temperature profiles are shown in Fig. 7. The total flow rate is 7767 b/d. The changes in temperature profiles in horizontal wells are limited if the flow rate is small or if the pressure drop along the well is small. Overall pressure drop in the well is only about 7 psi and the temperature change is 0.04 ^{o}F as shown in the figures. The matched curves are also depicted in Fig. 7. Since the resolution of temperature is restricted to 0.01 ^{o}F, temperature profile is discretized. Yet, the observed and inverted profiles closely matched. Fig. 8 shows the inverted permeability distribution and flow rate profile. Despite the small changes of pressure and temperature along the well, the inverted profile reproduced the feature of the true profile quite well.

Fig. 9 shows the observed profiles with the permeability distribution of case B. The total flow rate is 7842 b/d. Also, the pressure drop (15 psi) and temperature changes (0.07 ^{o}F) are very limited. The obtained matches are very close. The inverted permeability distribution and flow rate are compared with the true distribution in Fig. 10. In Fig. 10a, the low permeability zone near the toe is well represented but the inversion of the high permeability zone near the heel shows some differences. However, the overall permeability prediction is good and the obtained flow rate profile (Fig. 10b) shows a close match.

Single-phase gas production. Now we perform the permeability inversion with single-phase gas production. The well used for the calculation is the same and the bottomhole pressure is set at 3980 psi this time. Fig. 11 shows the observed pressure and temperature profiles with the inverted curves for the case A permeability profile in Fig. 6b. The total flow rate at the surface is 8449 MSCF/d. The pressure drop in the horizontal well is about 1.4 psi and the overall temperature change is 0.02 ^{o}F. Both the inverted temperature and pressure curves give a very close match to the observations. The inverted permeability and flow rate profiles are shown in Fig. 12. Even though the changes along the well are small, the inverted permeability and flow rate profiles capture the features of the true profiles well.

With the true permeability profile of case B, the total production is 8529 MSCF/d. The total pressure drop in the well is about 1 psi and the total temperature cooling is 0.02 ^{o}F. Fig. 13 shows the observed profiles and the matched curves. Both pressure and temperature profiles are closely matched. The inverted results are depicted in Fig. 14. The inverted permeability gives a profile close to the true except for near the heel region. Although the temperature profile is matched very well, the change itself is limited and is not captured by the measurement. If the measurement resolution were high, the temperature drop caused by high permeability zone near the heel would appear clearly and a better permeability distribution could be inverted.

Water entry detection. When water is produced, we can detect its entry from the wellbore temperature cooling if the water and oil are produced from the same level (same boundary temperature). We show a water entry example of water entering from two regions (900 – 1100 ft, and 1600 – 1800 ft from heel) and invert the permeabilities of these zones.

We consider a permeability profile as shown in Fig. 15. Two water entry zones are indicated in the figure. Observations generated based on this permeability field are shown in Fig. 16. The well with large diameter described in Table 2 is used and the bottomhole pressure is set as 3600 psi. As depicted in Fig. 16a, we have two water entry zones: one at the middle and the other near the toe of the well. For each water entry zone, the wellbore temperature is cooled as shown in Fig. 16c, while the pressure profile (Fig. 16b) does not show any signs of water entries. For this case, both water entry zones have equal permeability.

We inverted the permeabilities of the water entry zones and the permeabilities of the oil producing zone by matching the pressure and temperature profiles, and the flow rates of oil and water. The matched temperature and pressure curves are displayed in Fig. 17 and the inverted permeability distribution and flow rate profile are in Fig. 18. Both the temperature and pressure profiles are closely fitted by the inversion method. As a consequence, we were able to reproduce the permeability and flow rate profiles for the two water entry zones very accurately.

Gas entry detection. Similarly to water entry, gas entry cools the wellbore. However, the cooling effect by gas is much larger than that of water because the gas temperature actually cools off below the geothermal temperature while oil and water warm up. Therefore, the detection of gas is relatively easy. In this study, we show an example of the permeability inversion when oil and gas are produced. Again, we consider two gas entry regions: one is located near the toe (1,600 – 1,800 ft from heel) and the other one is at the middle (900 – 1,100 ft from heel). The well properties are the same as the water entry example except for bottomhole pressure which is set at 3900 psi.

We consider the two gas entry zones having the same permeability (20 md) while the oil permeability is 200 md as shown in Fig. 19. The observations (flow rate, pressure, and temperature profiles) from this permeability distribution are shown in Fig. 20. As can be found from Fig. 20a, gas entered into the well from two regions. Similarly, whereas we cannot see any indications of gas production on the pressure profile (Fig. 20b), the locations of gas entries can be found from the

temperature profile by detecting the temperature drop as depicted in Fig. 20c. We give the total flow rates of each phase, and pressure and temperature profiles to the inversion process as input data in this case as well.

The matched pressure and temperature profiles are shown in Fig. 21 and the inverted permeability and flow rate distributions are shown in Fig. 22 with the initial permeability distribution used to start the inversion. We slightly missed matching the pressure profile near the toe but the other zone and entire temperature profile are very closely matched. The obtained permeability distribution is close to the true permeability distribution. While the oil flow rate profile is successfully reproduced, gas flow rate replication shows a small difference from the observation. However, more importantly, the permeabilities of both gas entry zones were predicted accurately.

Field example. We use the temperature and pressure profiles measured in a horizontal well in the North Sea which is producing oil and water to test the inversion method with actual well data. We applied the inversion method to the field data and obtained flow rate profiles of oil and water by matching the temperature and pressure data.

The well is not perfectly horizontal and has slight deviations along its path, as shown in the well trajectory (Fig. 23). The total oil production rate is 12,700 b/d and the water production rate is 8,600 b/d. According to the interpretation of the spinner flowmeter and other logs run on this well, from the interval between measured depths of 10689 ft to 9785 ft, 4,100 b/d oil is being produced with 2,200 b/d of water. From 9,705 ft to 8712 ft, the oil production rate is 8,600 b/d and the water production rate is 6,600 b/d. About 65% of the total production is produced from the upper zone. The measured temperature and pressure profiles along this upper zone are shown in Fig. 24.

The temperature profile (Fig. 24a) shows a noticeable temperature drop from about 9,200 – 9,600 ft, measured depth, indicating that this is a water producing zone. The available properties given for this well are listed in Table 3. For the other properties we need for calculations, we use the values listed in Tables 1 and 2. From this data, and assuming water production from 9200 to 9600 feet measured depth, the inverted temperature and pressure profiles shown in Fig. 25 were obtained. The inverted flow rate profiles that yielded these temperature and pressure profiles are shown in Fig. 26.

Although the inverted temperature deviated from the observation around 8500 ft measured depth, the overall inversion is good. The pressure curves also show close agreement. Most importantly, the water and oil flow rates obtained from the inversion of the temperature and pressure profiles agreed very closely with the production log-derived oil and water production rates from the upper zone in this well. As can be seen from the figure, oil is produced mainly from 9,000 – 9,200 ft and 8,400 – 8,500 ft. The oil production from 9,000 – 9,200 feet causes the temperature increase observed along this section. The oil producing zone at 8,400 – 8,500 feet causes the increase in the wellbore pressure gradient in this section. By matching both the temperature and pressure profiles, the inversion method reveals both of these oil inflow regions.

Summary and Conclusions

This study presented an inversion method that interprets distributed temperature and pressure data to obtain flow rate profiles along horizontal wells. We have applied the inversion method, which is based on the Levenberg-Marquardt algorithm, to minimize the differences between the measured profiles and the profiles calculated from the prediction model developed. Through numerical experiments, we inferred the relative importance of the input data and determined the best combination of input data.

We have shown synthetic and field examples to illustrate how to use the inversion model to interpret the flow profile of a horizontal well. The synthetic examples showed that even with single-phase oil production, the inflow profile may be estimated. The method is even more robust when water or gas is produced along discrete intervals in an oil production well because of the unique temperature signature of water or gas production.

We have applied the inversion method to temperature and pressure profiles measured with production logs in a North Sea horizontal oil and water producing well. With the inversion method developed, we have successfully matched the profile of temperature and pressure to determine the inflow profiles of oil and water.

Acknowledgements

The authors are grateful for the financial support of the U.S. Department of Energy through Contract Number DE-FC26-03NT15402. A. D. Hill holds the Robert L. Whiting Endowed Chair at Texas A&M University.

Nomenclature

C_p	specific heat capacity
d	derivative vector
D	weight matrix
e	error component vector
k	permeability
K_T	total thermal conductivity of rock and fluid
H	Hessian matrix
I	Identity matrix
J	Jacobian matrix
p	pressure
p_R	reservoir pressure
q	flow rate
r_w	wellbore radius
T	temperature
u	Darcy velocity vector
w	parameter vector

$\mathbf{x}$	observation space
$\mathbf{y}$	observations
β	thermal expansion coefficient
μ	viscosity
ρ	density

Subscripts

c	calculated
D	dimensionless
j,k	position index
l	liquid
m	measured

References

1. Kragas, T. K., Williams, B. A., and Myers, G. A.: "The Optic Oil Field: Deployment and Application of Permanent In-Well Fiber Optic Sensing Systems for Production and Reservoir Monitoring," paper SPE 71529 presented at the 2001 SPE Annual Technical Conference and Exhibition, New Orleans, 30 September-3 October.
2. Fryer, V. *et al.*:"Monitoring of Real-Time Temperature Profiles Across Multizone Reservoirs during Production and Shut in Periods Using Permanent Fiber-Optic Distributed Temperature Systems," paper SPE 92962 presented at the 2005 SPE Asia Pacific Oil and Gas Conference and Exhibition, 5-7 April, Jakarta, Indonesia.
3. Brown, G. et al.:"Production Monitoring Through Openhole Gravel-Pack Completions Using Permanently Installed Fiber-Optic Distributed Temperature Systems in the BP-Operated Azeri Field in Azerbaijan," paper SPE 95419 presented at the 2005 SPE Annual Technical Conference and Exhibition, 9-12 October, Dallas.
4. Nath, D.K. *et al.*:"Real-Time Fiber-Optic Distributed Temperature Sensing (DTS) – New Applications in the Oil Field," paper SPE 103069 presented at the 2006 SPE Annual Technical Conference and Exihibition, 24-27 September, San Antonio.
5. Falcone, G., Hewitt, G.F., Alimonti, C., and Harrison, B.: "Multiphase Flow Metering : Current Trends and Future Developments," *JPT* (April 2002) 77.
6. Brown, G.: "Monitoring Multilayered Reservoir Pressures and Gas/Oil ratio Changes Over Time Using Permanently Installed Distributed Temperature Measurement," paper SPE 101886 presented at the 2006 SPE Annual Technical Conference and Exhibition, San Antonio.
7. Johnson, D., Sierra, J., Kaura, J., and Gualtieri, D.: "Successful Flow Profiling of Gas Wells Using Distributed Temperature Sensing Data," paper SPE 103097 presented at the 2006 SPE Annual Technical Conference and Exihibition, 24-27 September, San Antonio.
8. Marquardt, D.W.: "An Algorithm for Least-Squares Estimation of Nonlinear Parameters," *J. of the Society for Industrial and Applied Mathematics* (June 1963) 431.
9. Yoshioka, K., *et al.*: "A Comprehensive Model of Temperature Behavior in a Horizontal Well," paper SPE 95656 presented at the 2005 SPE Annual Technical Conference and Exhibition, Dallas, 9-12 October.
10. Dawkrajai, P.: "Temperature Prediction Model for a Producing Horizontal Well," PhD dissertation, U. of Texas, Texas (2006).
11. Yoshioka, K. *et al.*: "Predtion of Temperature Changes Caused by Water or Gas Entry into a Horizontal Well," SPE 100209 accepted for publication in *SPEPO*.
12. Hill, A.D.: *Production Logging -Theoretical and Interpretive Elements*, Society of Petroleum Engineers Inc., Richardson, TX, 1990.

Appendix A: Observation weights

We consider pressure and temperature profiles, and the total well flow rates of each phase as the primary inputs. In addition, we consider the spatial derivative of pressure and temperature profiles (dp/dx and dT/dx) since it has been observed that the slope of these curves sometimes indicates additional information[12].

In Eqs. 14-16, we introduced the weights for each observation. Each observation has different physical properties and units. Therefore, they should have different contributions to the objective function. For instance, if the weight of flow rate is improperly high compared to the other inputs, the inversion problem becomes identical to the problem of simply matching the flow rate data only.

In this study, we approximately equalize the sensitivities of the input data to the permeability estimation with observation weights to quantify the relative importance. Also, we treat the input data of the same kind equally. Threefore, for instance, the component of weight matrices $\left(\mathbf{D}_p\right)_{jj}$ can be replaced with simply D_p for all pressure observations. Since each observation has different units, we introduce dimensionless observation as follows.

$$q_{D,i} = \frac{q_i \mu}{k p_R \Delta x}, \tag{A.1}$$

$$p_{D,j} = \frac{p_j}{p_R}, \tag{A.2}$$

$$T_{D,j} = \frac{T_j}{\rho C_p p_R}, \tag{A.3}$$

$$x_D = \frac{x}{r_w}. \tag{A.4}$$

where Δx is the length of the segment.

The sensitivity of the dimensionless observation $p_{D,j}$ to the permeability of the kth segment k_k can be written as $\partial p_{D,j} / \partial k_k$. To obtain similar contributions from different observations, we equate the sensitivities with the weights. Then we have

$$\frac{1}{D_p^{1/2}}\frac{\partial k_k}{\partial p_{D,j}} = \frac{1}{D_T^{1/2}}\frac{\partial k_k}{\partial T_{D,j}} = \frac{1}{D_q^{1/2}}\frac{\partial k_k}{\partial q_{D,j}} = \frac{1}{D_{dp}^{1/2}}\frac{\partial k_k}{\partial (dp_D/dx_D)_j} = \frac{1}{D_{dT}^{1/2}}\frac{\partial k_k}{\partial (dT_D/dx_D)_j}, \quad \text{(A.5)}$$

where D_{dp} and D_{dT} are the weights for dp/dx and dT/dx.

From Eq. A.5, the relative sensitivity of the dimensionless pressure observation to the flow rate can be written as

$$\frac{D_q^{1/2}}{D_p^{1/2}} = \frac{\partial k_k/\partial q_{D,i}}{\partial k_k/\partial p_{D,j}} = \frac{\partial p_{D,j}}{\partial q_{D,j}}. \quad \text{(A.6)}$$

Therefore, the relationship between D_p and D_q is given by

$$D_q = \left(\frac{\partial p_{D,j}}{\partial q_{D,i}}\right)^2 D_p. \quad \text{(A.7)}$$

$\partial p_{D,j}/\partial q_{D,i}$ is the sensitivity of $q_{D,i}$ to $p_{D,j}$. Flow rate of the phase i is given by

$$\sum_{k=1}^{N} J_k (p_R - p_k) = q_i. \quad \text{(A.8)}$$

To estimate the sensitivity, we consider small perturbations of pressure and flow rate caused by, say, permeability and the resulting changes can be written as

$$p_j = p_j{}^0 + \delta p_j, \quad \text{(A.9)}$$

$$q_i = q_i{}^0 + \delta q_i, \quad \text{(A.10)}$$

where $p_j{}^0$ and $q_i{}^0$ are the initial pressure and flow rate before perturbations. The change in the flow rate is

$$\delta q_i = q_i - q_i{}^0 = \sum_{k=1}^{N} J_k (p_R - p_k) - J_j \delta p_j - \sum_{k=1}^{N} J_k (p_R - p_k), = -J_j \delta p_j \quad \text{(A.11)}$$

Thus we have

$$\frac{\partial p_j}{\partial q_i} = -\frac{1}{J_j}. \quad \text{(A.12)}$$

In dimensionless form, the sensitivity becomes

$$\frac{\partial p_{D,j}}{\partial q_{D,i}} = \frac{k\Delta x}{\mu}\frac{\partial p_j}{\partial q_i} = -\frac{k\Delta x}{\mu J_j}. \quad \text{(A.13)}$$

Then the relative weight is

$$D_q = \left(\frac{k\Delta x}{\mu J_j}\right)^2 D_p. \quad \text{(A.14)}$$

Similarly, the weight of dimensionless temperature observation is given by

$$D_T = \left(\frac{\partial p_{D,j}}{\partial T_{D,j}}\right)^2 D_p. \quad \text{(A.15)}$$

If the well is horizontal and its surrounding temperature is constant, the physical relationship between wellbore temperature and pressure can be approximated as

$$\frac{dT_j}{dx} = K_{JT}\frac{dp_j}{dx}. \quad \text{(A.16)}$$

From Eq. A.16, we have

$$\frac{\partial p_j}{\partial T_j} = \frac{1}{K_{JT}}. \quad \text{(A.17)}$$

The dimensionless sensitivity is then

$$\frac{\partial p_{D,j}}{\partial T_{D,j}} = \frac{1}{\rho C_p}\frac{\partial p_j}{\partial T_j} = \frac{1}{\rho C_p}\left(\frac{1}{K_{JT}}\right) = \frac{1}{\beta T_j - 1} \cong -1. \quad \text{(A.18)}$$

Therefore, the weight for the dimensionless temperature is

$$D_T = (-1)^2 D_p = D_p. \quad \text{(A.19)}$$

What remain are the weights of $(dp_D/dx_D)_j$ and $(dT_D/dx_D)_j$. From Eq. A.5, we have

$$D_{dp} = \left(\frac{\partial p_{D,j}}{\partial (dp_D/dx_D)_j}\right)^2 D_p. \quad \text{(A.20)}$$

$(dp_D/dx_D)_j$ is actually calculated by the pressure difference across a segment divided by the length of the segment as

$$\left(\frac{dp_D}{dx_D}\right)_j = \left(\frac{\Delta p_D}{\Delta x_D}\right)_j = \frac{p_{D,j} - p_{D,j-1}}{\Delta x_D}, \quad \text{(A.21)}$$

With a small perturbation, the changes of $p_{D,j}$ and $(\Delta p_D/\Delta x_D)_j$ result in

$$p_{D,j} = p_{D,j}{}^0 + \delta p_{D,j}, \quad \text{(A.22)}$$

$$\left(\frac{\Delta p_D}{\Delta x_D}\right)_j = \left(\frac{\Delta p_D}{\Delta x_D}\right)_j^0 + \delta\left(\frac{\Delta p_D}{\Delta x_D}\right)_j . \quad (A.23)$$

Solving for the perturbed change of $(\Delta p_D/\Delta x_D)_j$ gives

$$\begin{aligned}\delta\left(\frac{\Delta p_D}{\Delta x_D}\right)_j &= \left(\frac{\Delta p_D}{\Delta x_D}\right)_j - \left(\frac{\Delta p_D}{\Delta x_D}\right)_j^0 \\ &= \frac{p_{D,j}{}^0 + \delta p_{D,j} - p_{D,j-1}}{\Delta x_D} - \frac{p_{D,j}{}^0 - p_{D,j-1}}{\Delta x_D} . \\ &= \frac{\delta p_{D,j}}{\Delta x_D}\end{aligned} \quad (A.24)$$

Therefore, we obtain

$$\frac{\partial p_{D,j}}{\partial\left(dp_D/dx_D\right)_j} = \Delta x_D , \quad (A.25)$$

Substituting into Eq. A.20, the weight for D_{dp} is then given as

$$\begin{aligned}D_{dp} &= \left(\frac{\partial p_{D,i}}{\partial\left(dp_D/dx_D\right)_j}\right)^2 D_p . \\ &= \left(\Delta x_D\right)^2 D_p\end{aligned} \quad (A.26)$$

Similarly to $(\Delta p_D/\Delta x_D)_j$, the weight for $(dT_D/dx_D)_j$ is

$$D_{dT} = \left(\Delta x_D\right)^2 D_T . \quad (A.27)$$

Appendix B: Effects of Input Data Choice

The possible candidates for input data are the pressure profile, the temperature profile, the flow rate, the pressure derivative, and the temperature derivative. Total well flow rate will be given as an observation for every case. Through numerical examples, we evaluate the effects of each input data on the inversion results. The experiments were conducted for single-phase oil production and single-phase gas production with a variety of permeability distributions.

We considered four different distributions (cases A, B, C, and D) along the horizontal well as shown in Fig. 6 for single-phase oil and single-phase gas production examples. High permeability zone and low permeability zones are located alternately in different ways. To obtain larger wellbore effects on the profiles, the well with small diameter described in Table 2 is used in the experiments and the bottomhole (heel) pressure is set for 3,600 psi for the oil production and 3,900 psi for the gas production. The reservoir whose properties are listed in Table 1 is considered.

For all the cases, we evaluate the effect of input data given on the inversion calculation. The combinations we give are: pressure only, temperature only, pressure and temperature, pressure and pressure derivative, temperature and temperature derivative, and all of them. We will determine the best combination among them through numerical experiments. As an example of additional input data effects, the generated observations of oil production case A and the matched curves by using pressure only, temperature only, and all the observations are shown in Fig. B.1.

Giving the pressure data only shows a close match with the pressure profile but the temperature curves did not match. That indicates that pressure could be matched even if its temperature profile is off from the observation. On the other hand, giving temperature only obtains a good match while the pressure profiles also match. With more input data (giving all possible input), no significant differences were seen. Fig. B.2 displays the inversion results from case A. As pressure data only did not show a good match, it is not surprising that inversion from pressure only did not predict the true permeability profile. However, other combination choices captured the features of the alternating permeability zone locations, and their inversion results show good resemblance to the true permeability distribution. Inverted flow rate profile from temperature and pressure data were compared with the observed one in Fig. B2c. Flow rate inversion was very successful.

The observed curves of gas case A and the matched curves are depicted in Fig. B.3. The choice of pressure data only shows a close match of the pressure curve while its temperature curve slightly deviates from the observation. On the other hand, the matched curves from temperature data only show poor matches for both pressure and temperature curves. These discrepancies can be seen more clearly in the derivative of the data. In this case, the choice of all input data provides better matches than these choices. The inversion of permeability results are shown in Fig. B.4. As expected, the results from the choices of pressure data only and temperature data only did not capture the features of the permeability profile well, while the combination of pressure and temperature and their derivatives gives a close match to the true permeability distribution. The obtained flow rate profile shows a very close match with the observed one.

We did the same experiments for the other permeability profile cases. Although we have not seen a generic rule of input parameter choices, a tendency may be obtained by summarizing permeability discrepancies between the true profiles and the predicted ones. We calculated *l-2* norm of the error as

$$Err = \sqrt{\sum_{j=1}^{20}\left(\frac{k_{j,true} - k_{j.inverted}}{k_{j,true}}\right)^2} , \quad (B.1)$$

where $k_{j,true}$ and $k_{j,inverted}$ are the true and the inverted permeability of the position j respectively. The obtained errors were normalized by dividing by the error of the result from pressure data for comparison reason. The average values of all the normalized errors from the cases are shown in Fig. B.5. The combination of temperature and pressure provides the least error above all the other choices. Therefore, we select temperature and pressure profiles as input data to the inversion process in addition to total flow rate in this study.

Table 1 Reservoir and fluid properties.

Reservoir			
Reservoir length [ft]	2000		
Reservoir width [ft]	3150		
Reservoir height [ft]	55		
Reservoir pressure [psi]	4000		
T at outer boundary [^{o}F]	180		
Fluid			
Specific gravity of gas	0.75		
Salinity of water [%]	5		
Oil API	45.176		
Dissolved GOR [SCF/STB]	800		
Surface tension [dyne/cm]	10		
	Oil	***Water***	***Gas***
K_{Tt} [Btu/hr ft °F]	2	2.5	1.3
K [Btu/hr ft ^{o}F]	0.0797	0.3886	0.0116

Table 2 Well properties.

	Small	***Large***
ID [in]	2.602	4
OD [in]	3.5	4.5
Diameter with cement [in]	5	6
K_{casing} [Btu/hr ft ^{o}F]	6.933	
K_{cement} [Btu/hr ft ^{o}F]	4.021	
Relative roughness	0.01	
Total Length [ft]	2000	
Pipe opened ratio [%]	2	

Table 3 Field properties

ID [in]	5
Total Length [ft]	1250
Reservoir height [ft]	89
T at outer boundary [^{o}F]	179.6
Specific gravity of gas	0.85
Oil API	37.8
Dissolved GOR [SCF/STB]	197
Reservoir pressure [psi]	2917

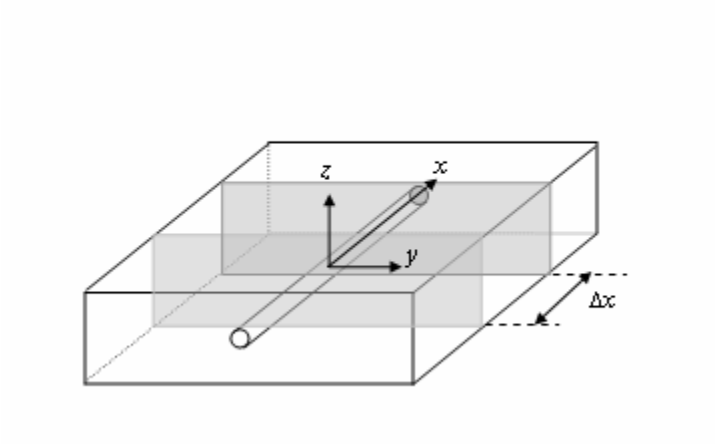

Fig. 1 Geometry of the forward model.

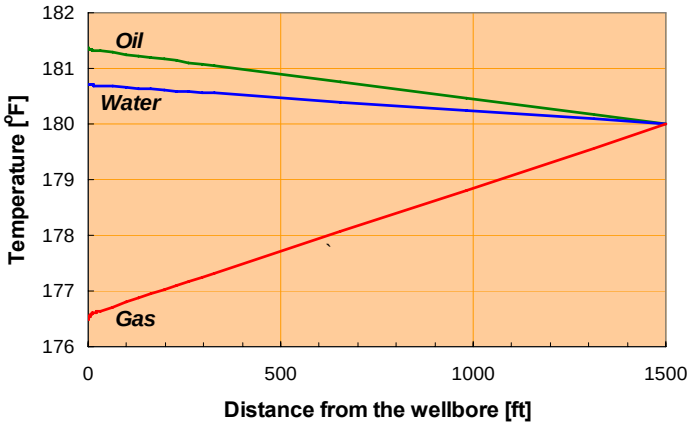

Fig. 2 Reservoir temperature profiles (different fluid type).

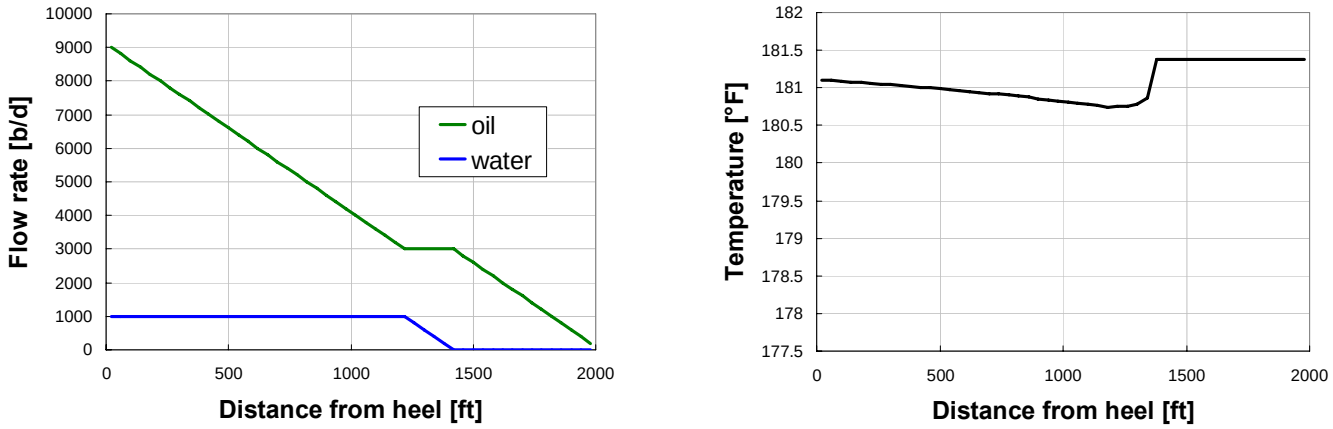

Fig. 3 Water entry case (a) flow rate and (b) temperature profile.

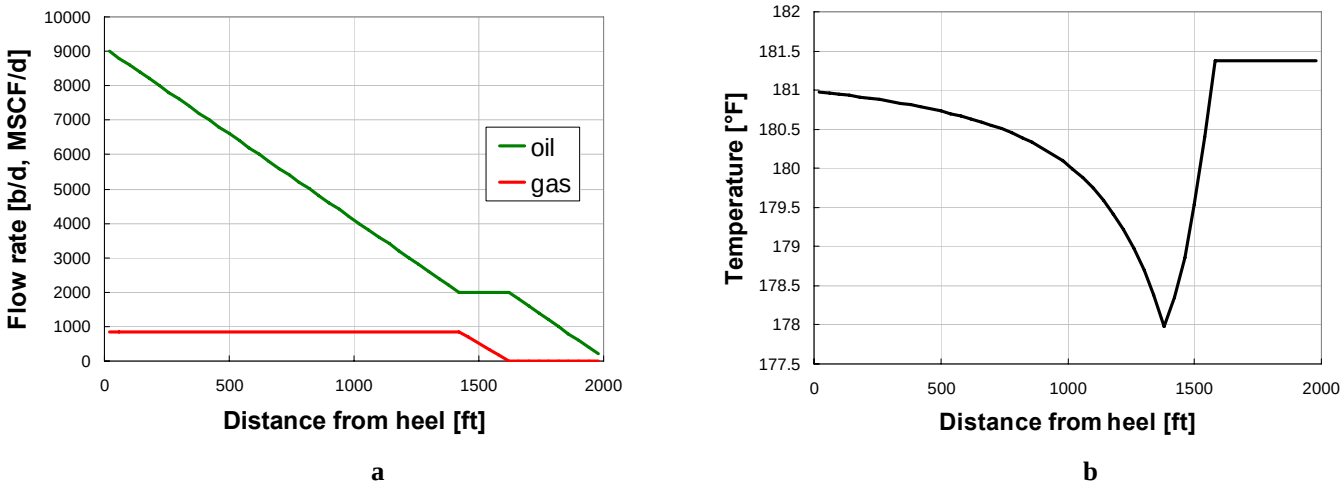

Fig. 4 Gas entry case (a) flow rate and (b) temperature profile.

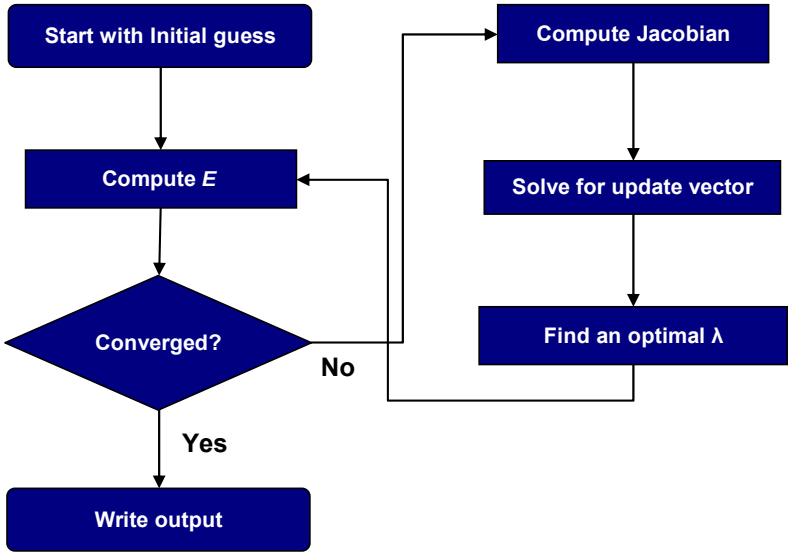

Fig. 5 Schematic of the inversion procedure.

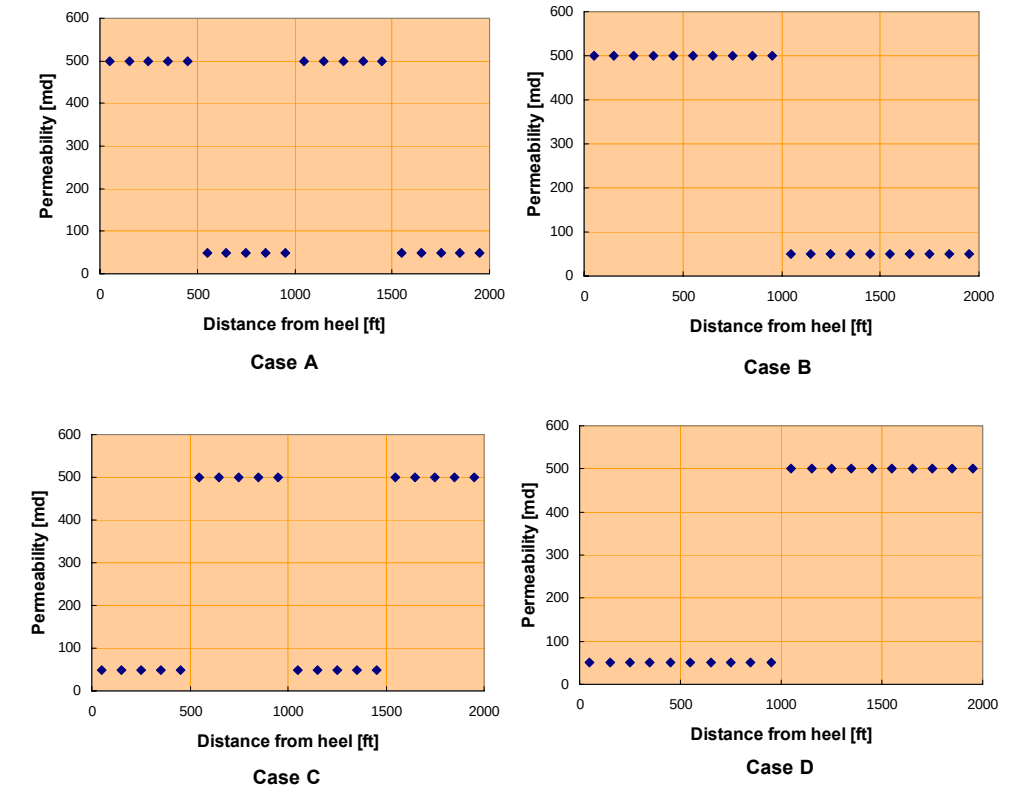

a

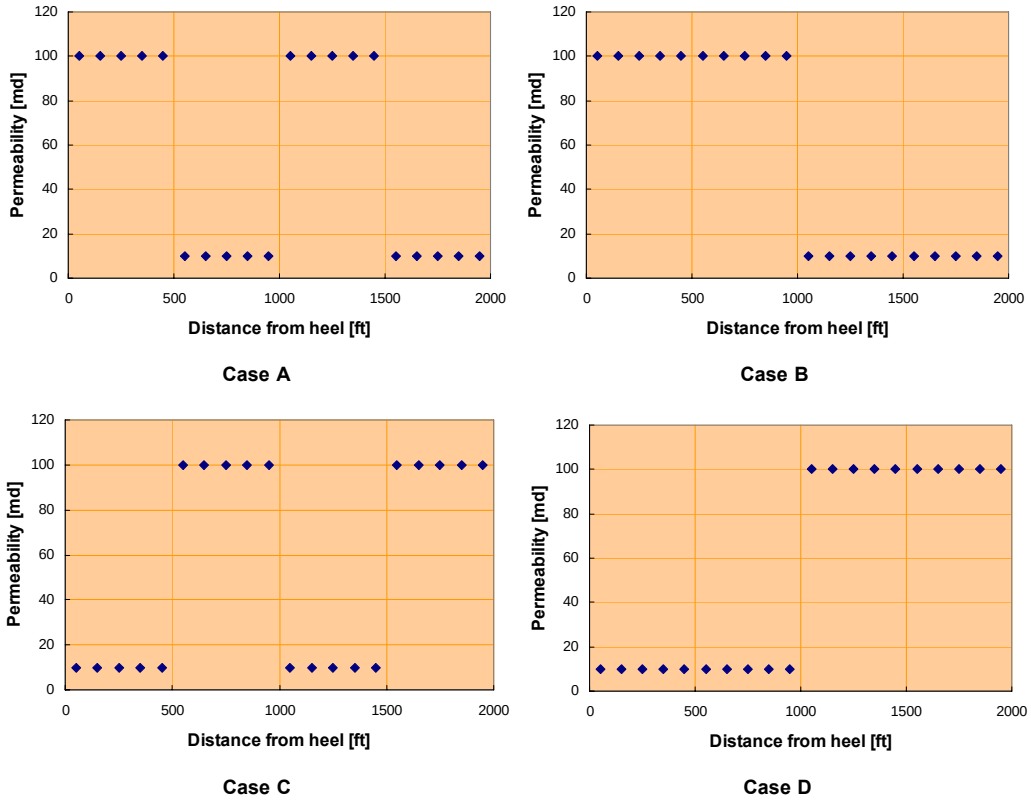

b

Fig. 6 Four different permeability distributions along horizontal well, (a) oil production cases and (b) gas production cases.

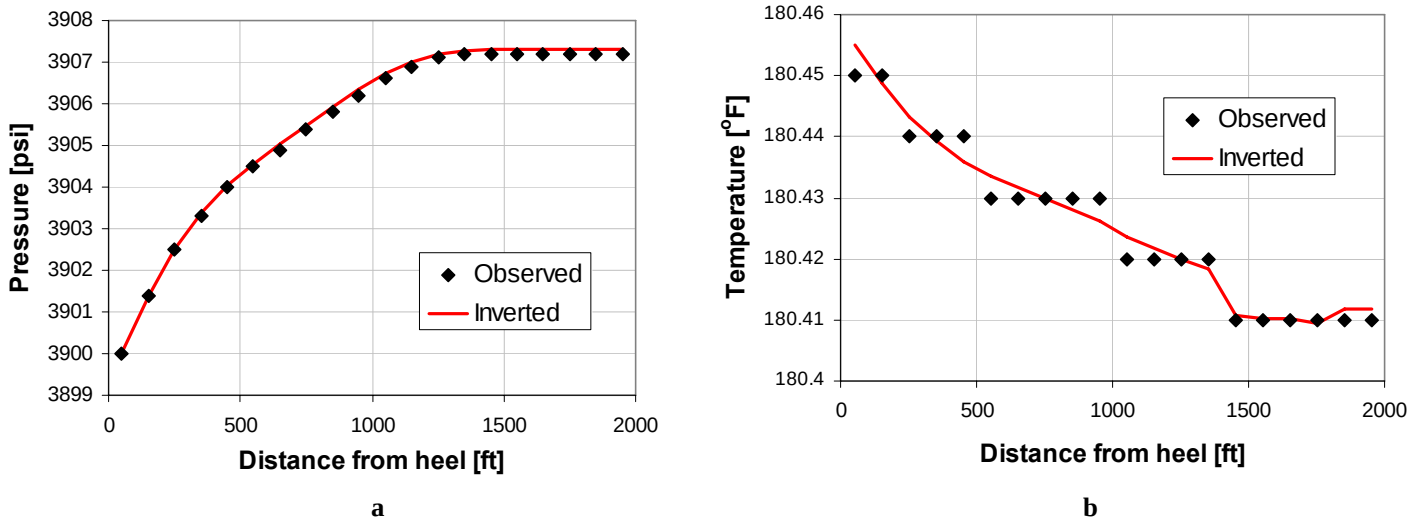

a b

Fig. 7 Observed and matched curves of (a) pressure and (b) temperature (case A, oil).

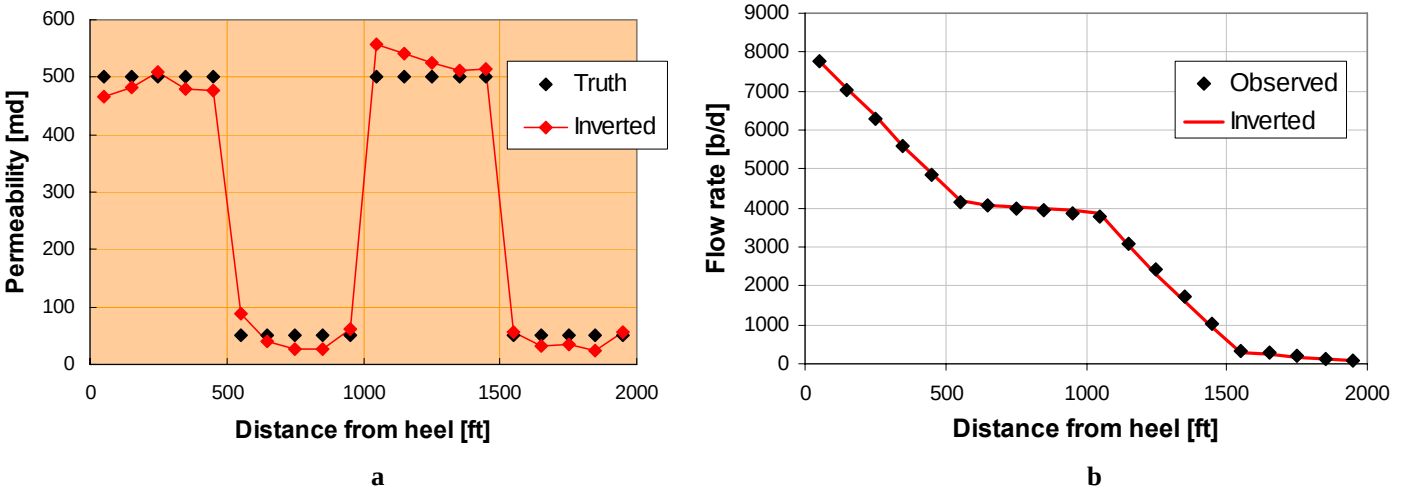

a b

Fig. 8 Inverted (a) permeability distribution and (b) flow rate profile (case A, oil).

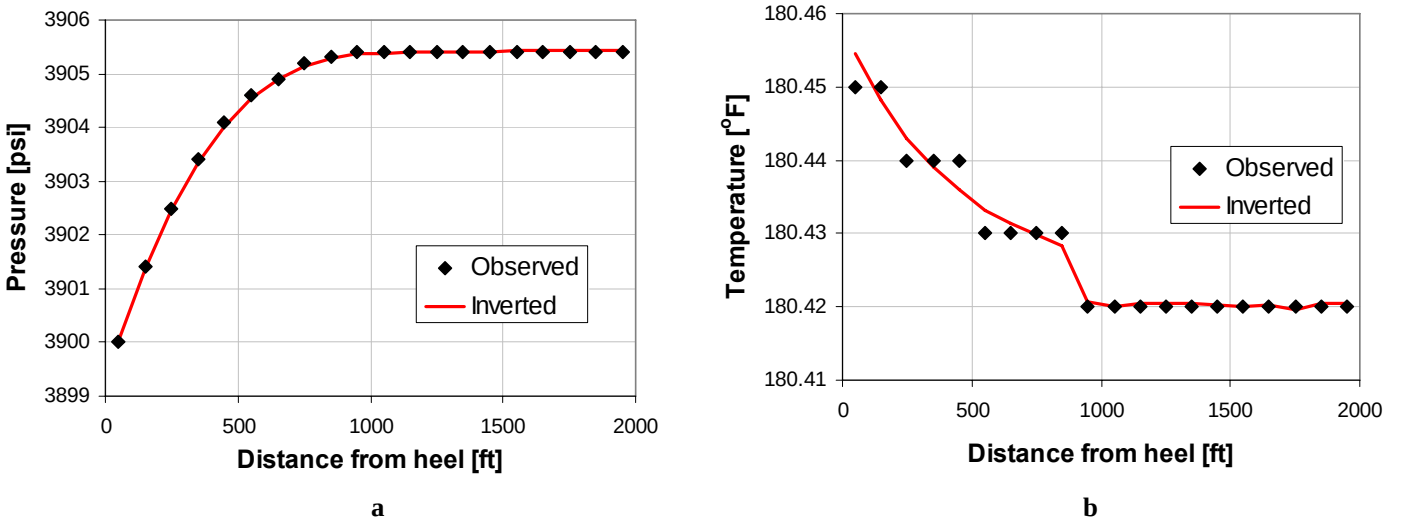

a b

Fig. 9 Observed and matched curves of (a) pressure and (b) temperature (case B, oil).

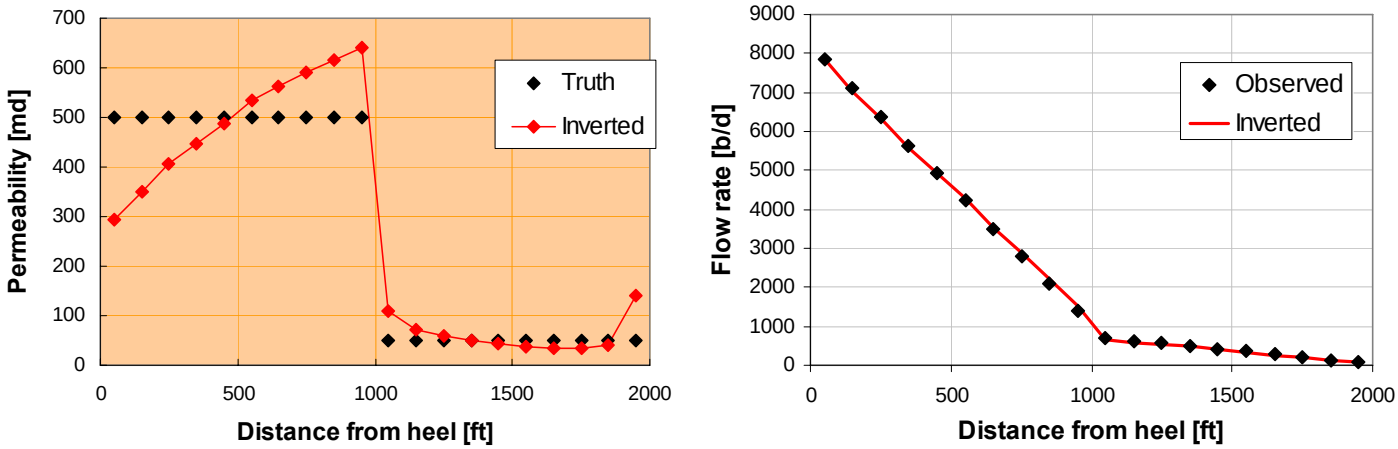

Fig. 10 Inverted (a) permeability distribution and (b) flow rate profile (case B, oil).

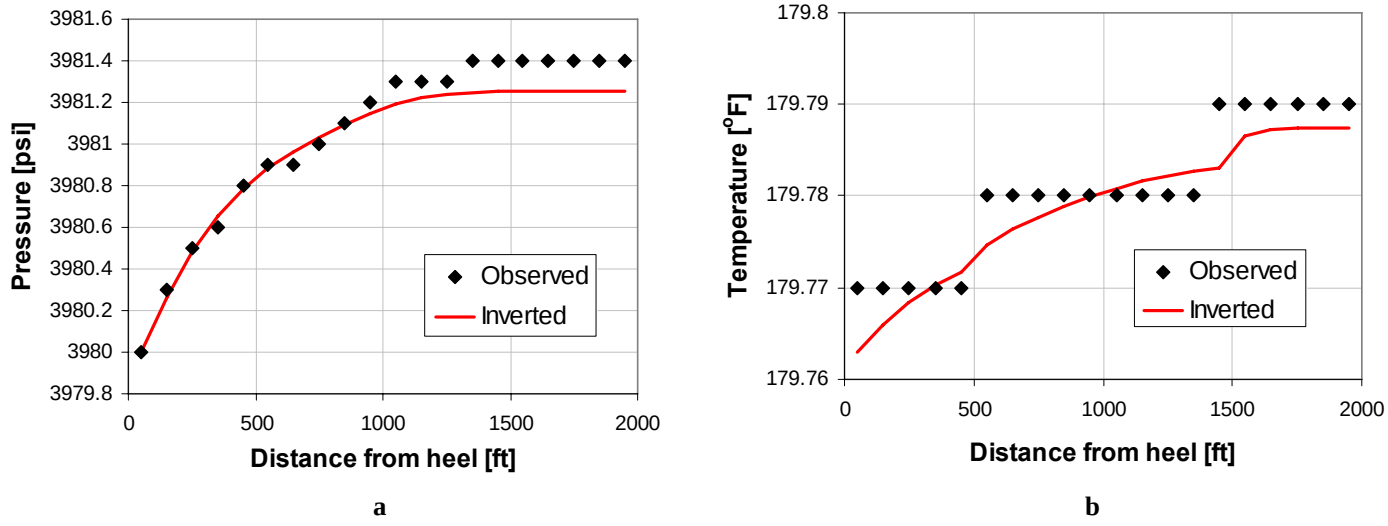

Fig. 11 Observed and matched curves of (a) pressure and (b) temperature (case A, gas).

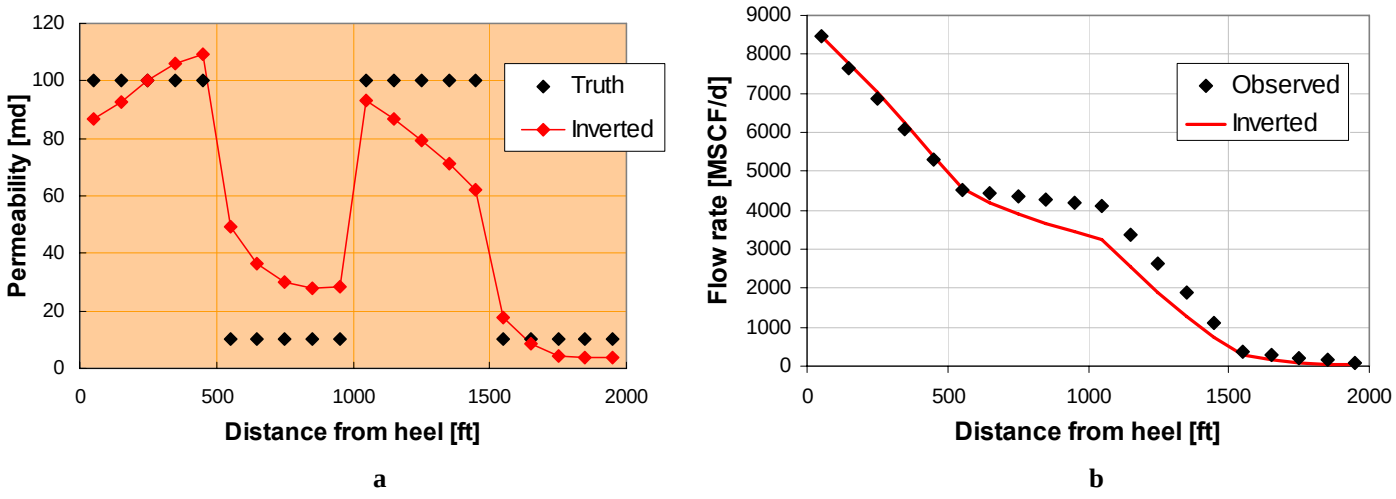

Fig. 12 Inverted (a) permeability distribution and (b) flow rate profile (case A, gas).

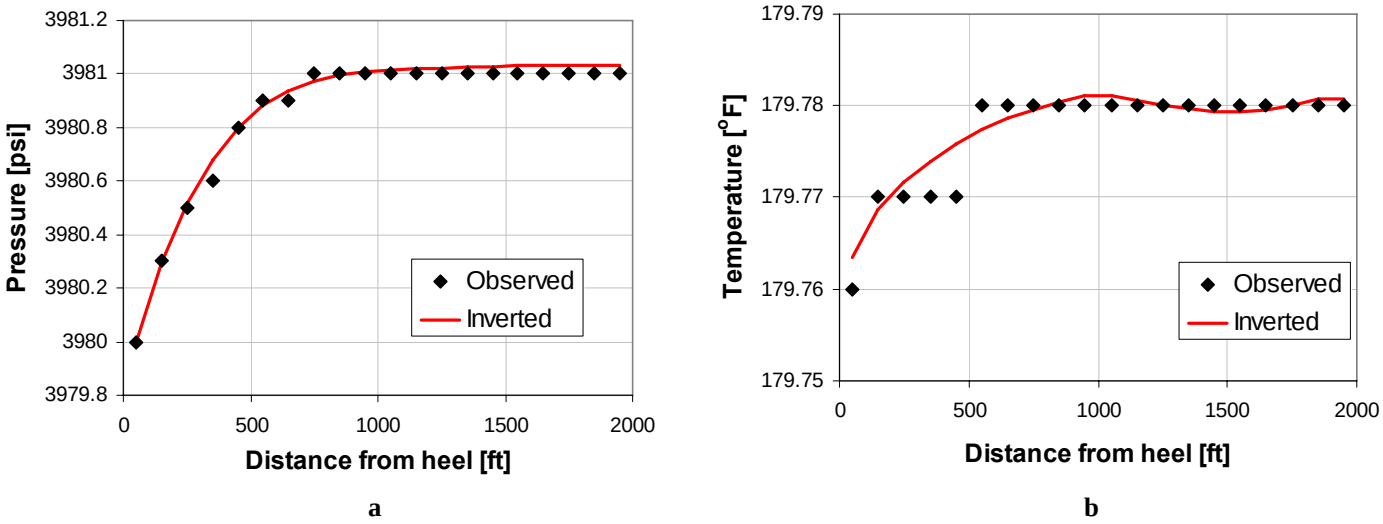

Fig. 13 Observed and matched curves of (a) pressure and (b) temperature (case B, gas).

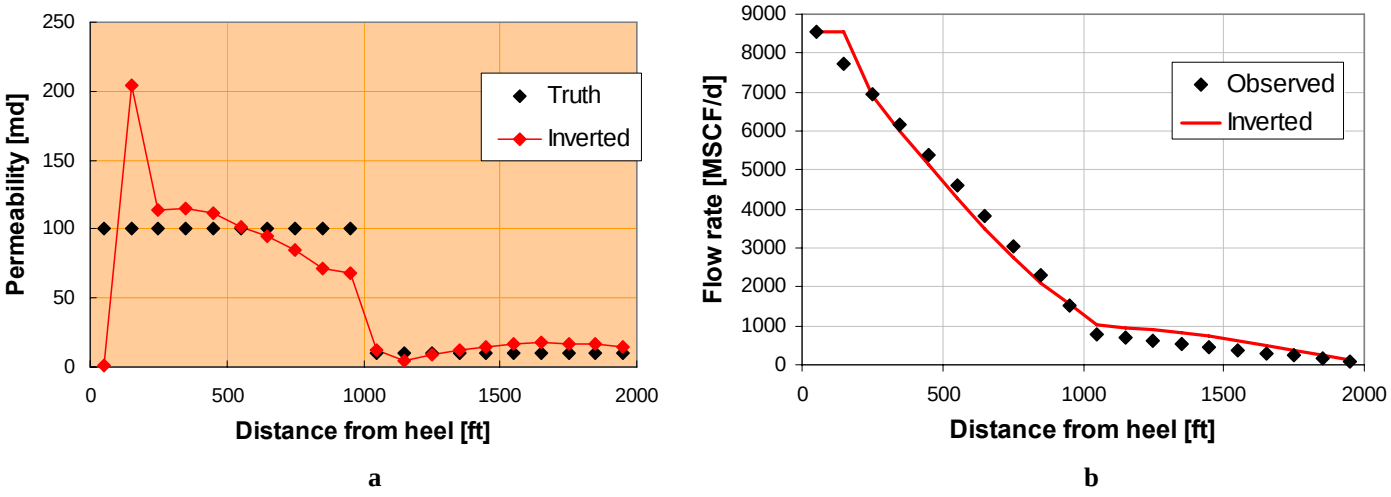

Fig. 14 Inverted (a) permeability distribution and (b) flow rate profile (case B, gas).

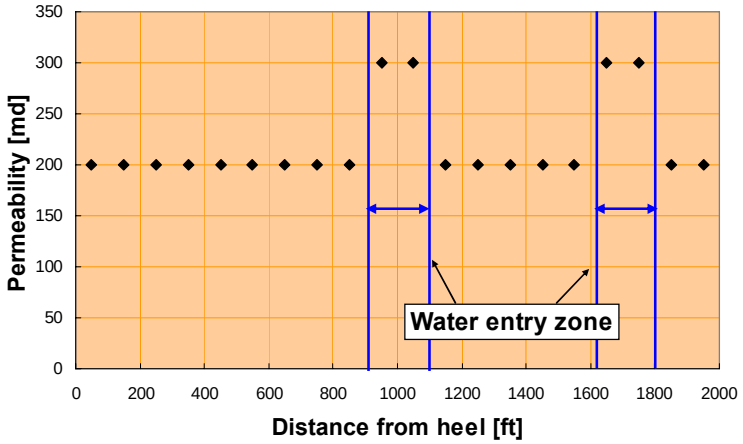

Fig. 15 Permeability distribution and water entry zones.

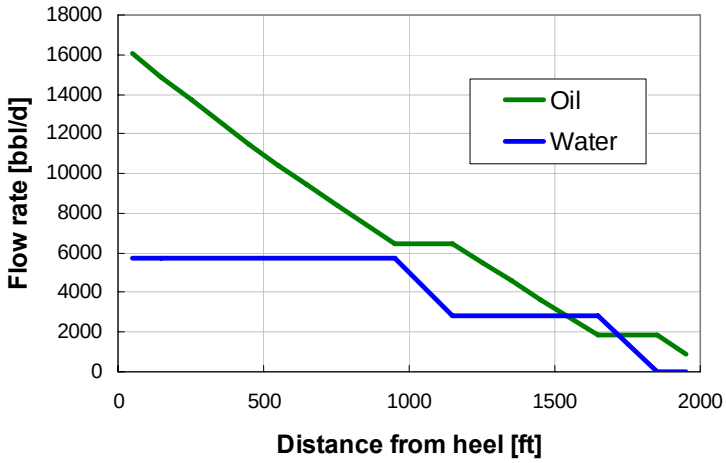

a

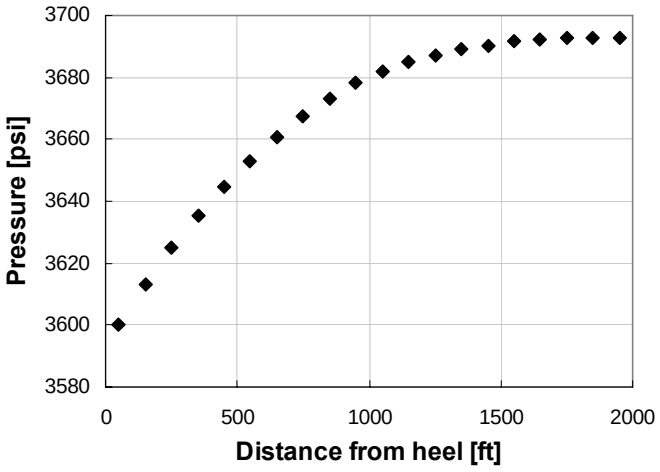

b

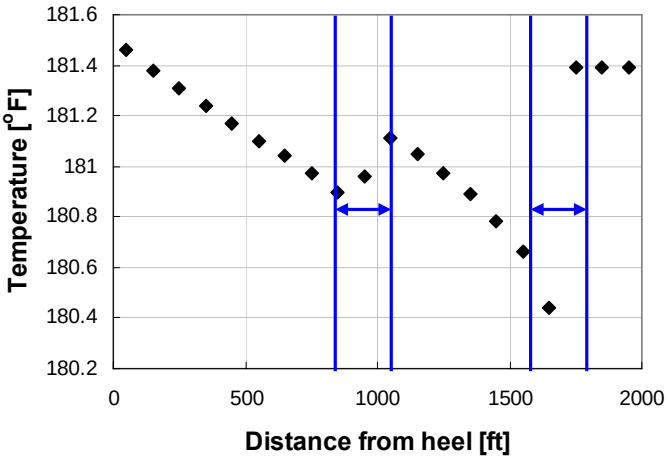

c

Fig. 16 Generated observations (a) flow rate, (b) pressure, and (c) temperature profiles.

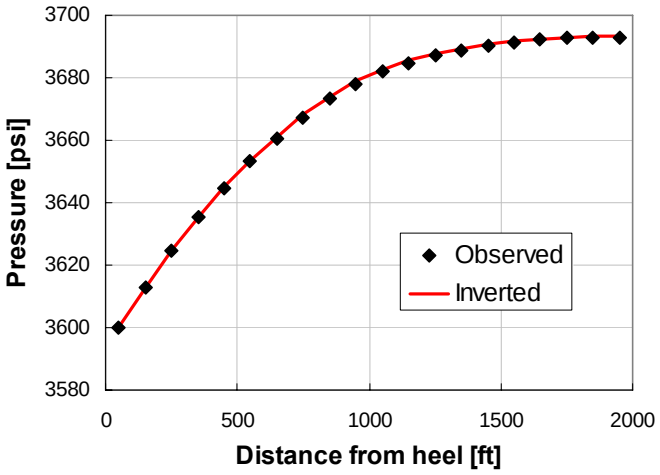

a

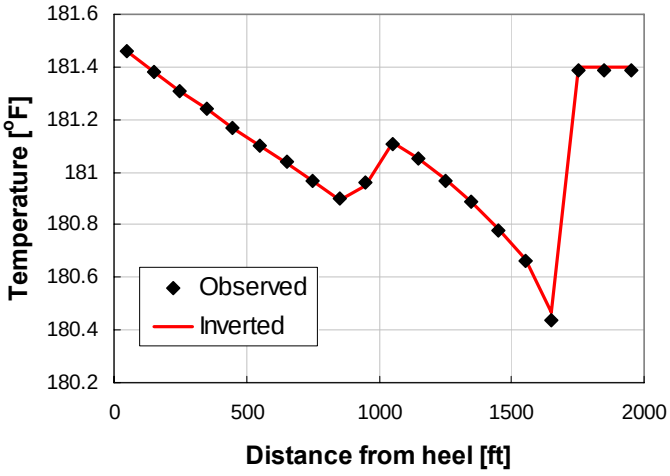

b

Fig. 17 Observations and matched curves (water entry).

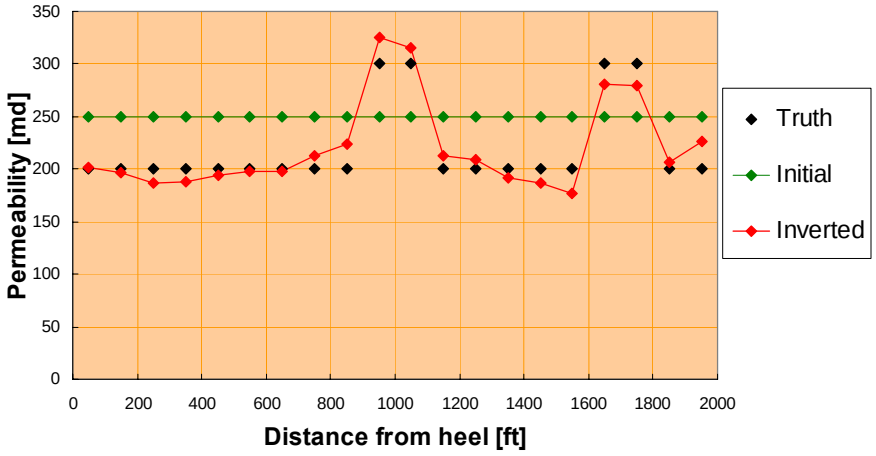

a

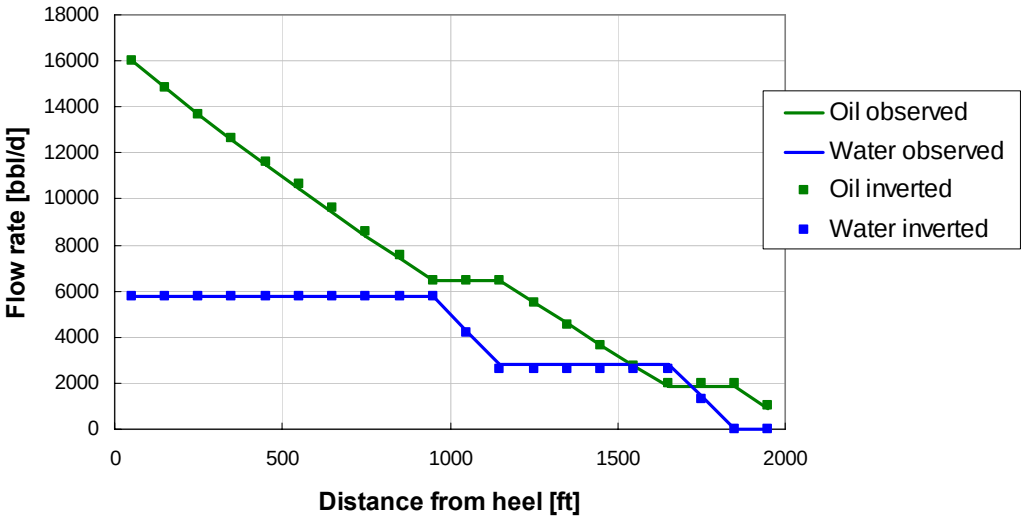

b

Fig. 18 Inverted (a) permeability distribution and (b) flow rate profiles (water entry).

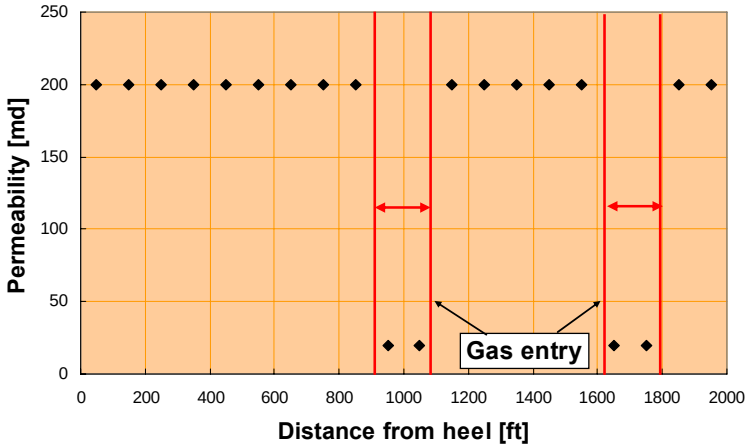

Fig. 19 Permeability distribution and gas entry zones.

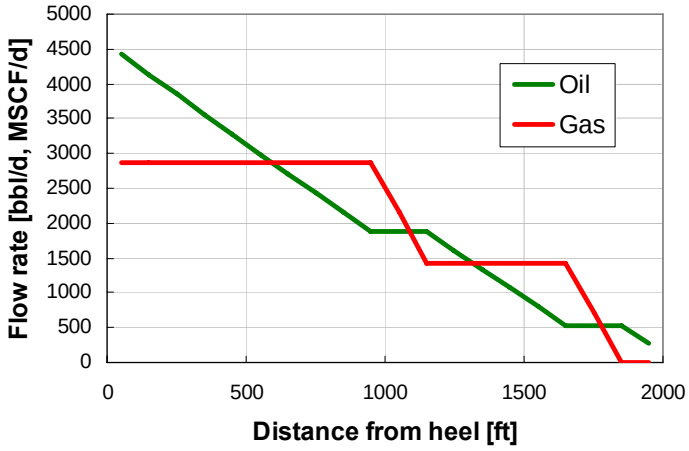

a

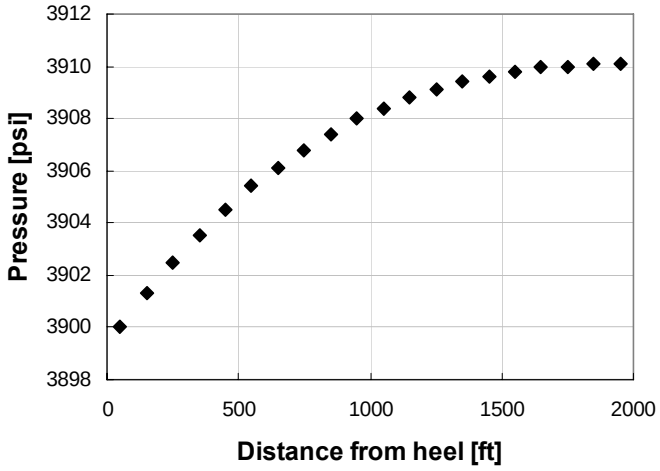

b

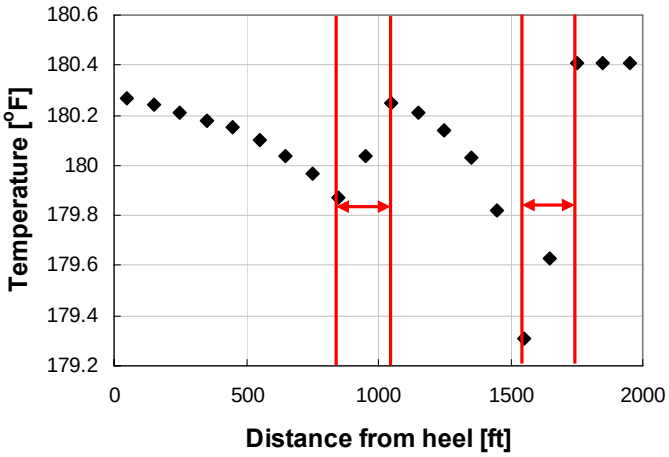

c

Fig. 20 Generated observations (a) flow rate, (b) pressure, and (c) temperature profiles.

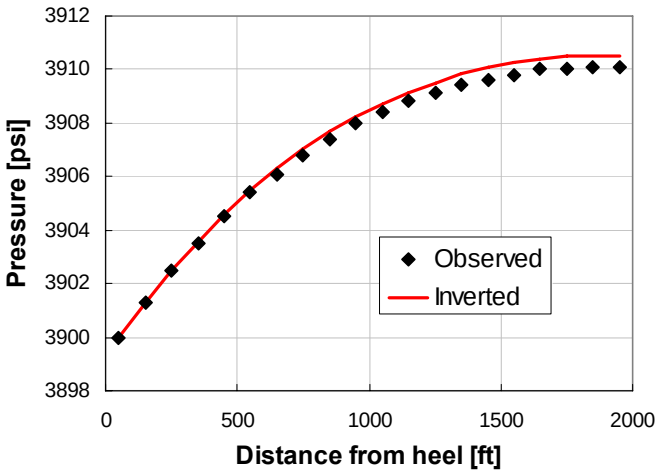

a

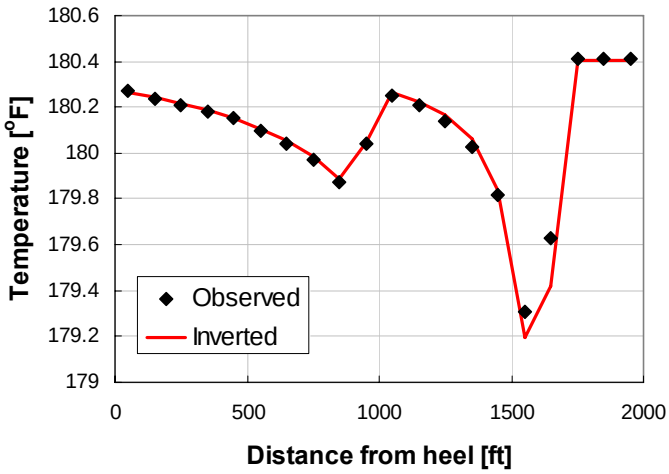

b

Fig. 21 Observations and matched curves (gas entry).

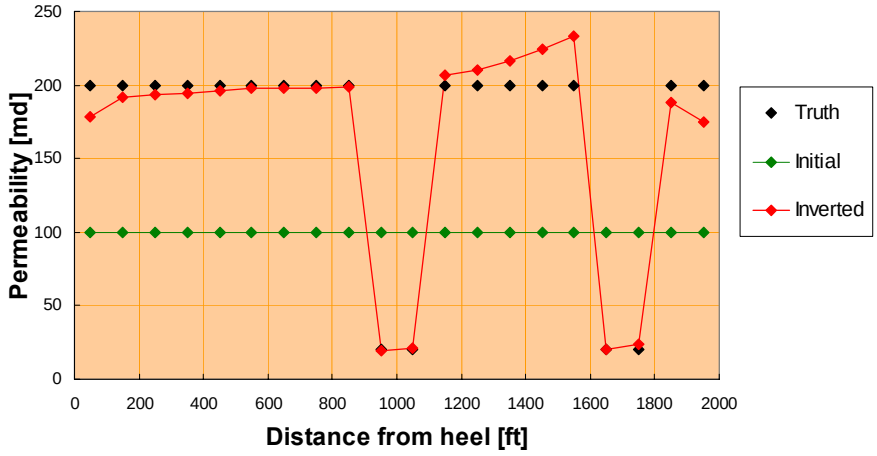

a

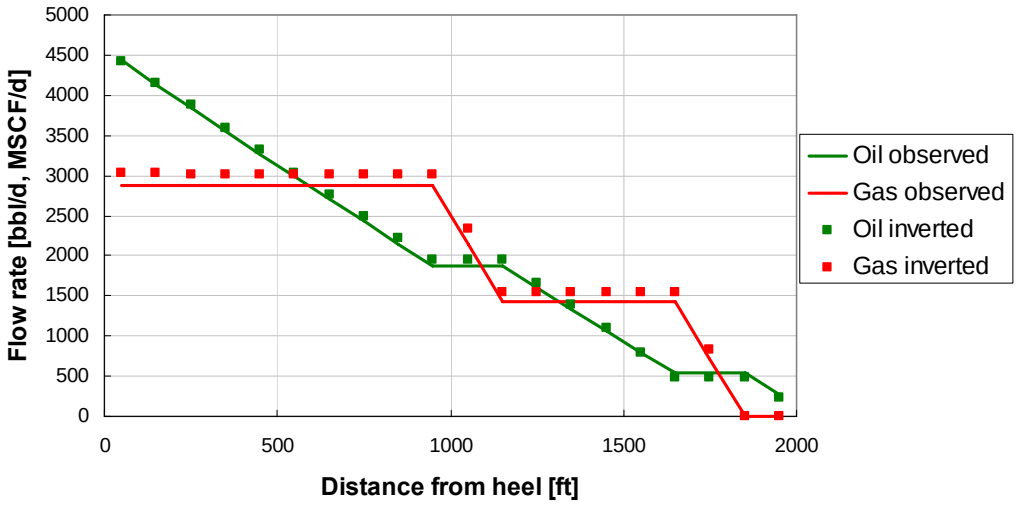

b

Fig. 22 Inverted (a) permeability distribution and (b) flow rate profiles (gas entry).

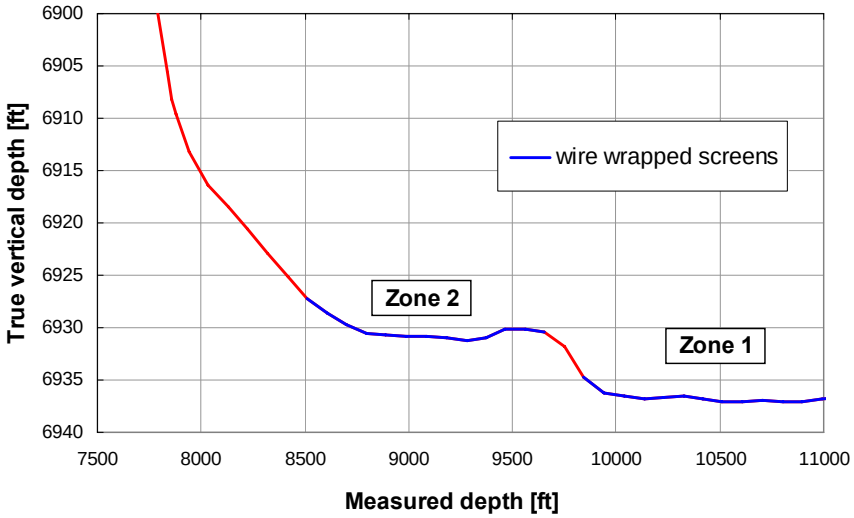

Fig. 23 Trajectory of the well.

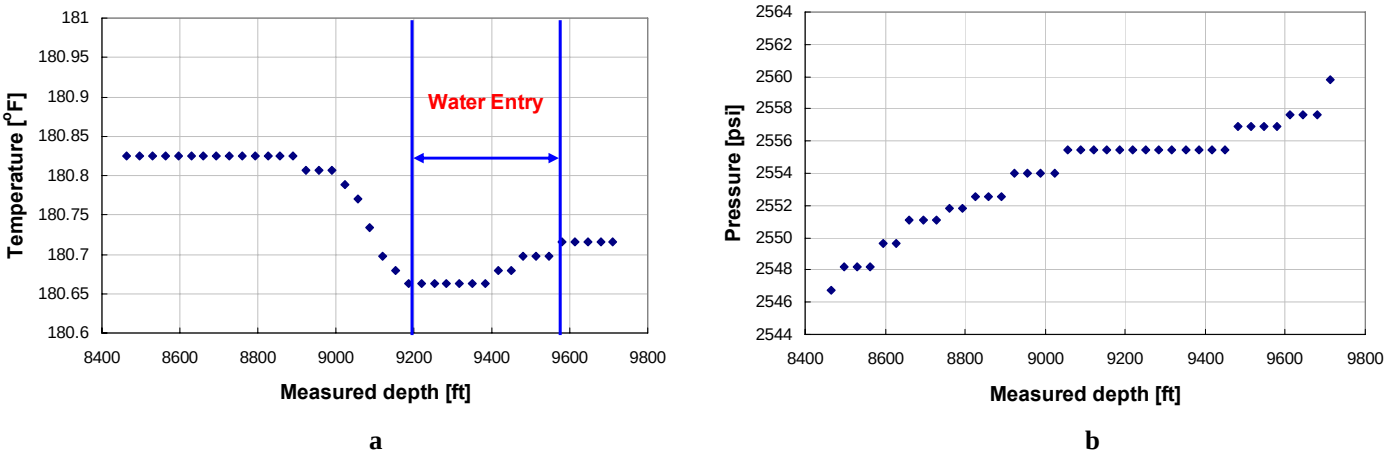

a b

Fig. 24 Measured profiles of (a) temperature, and (b) pressure.

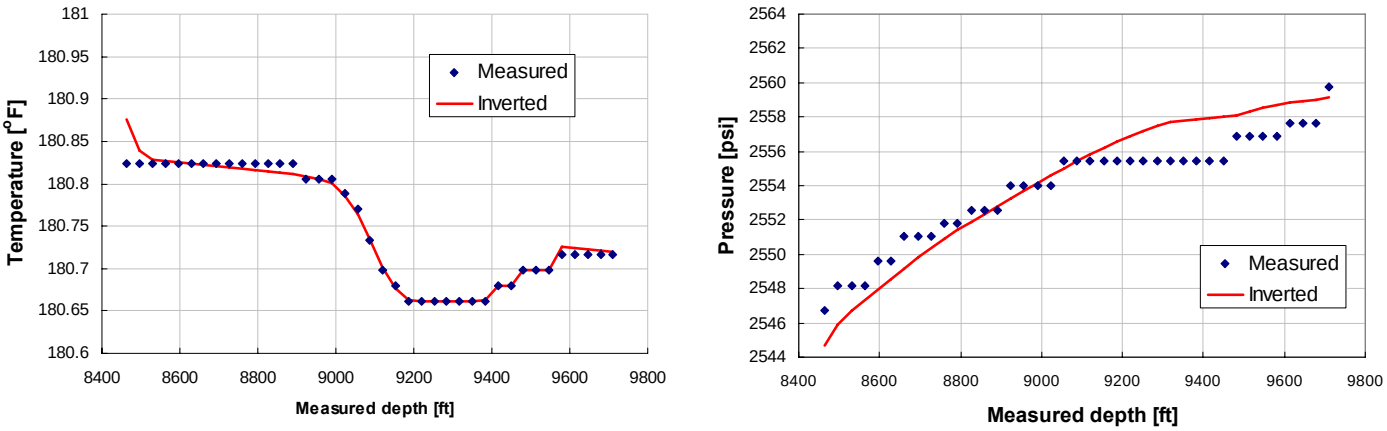

a b

Fig. 25 Inverted profiles of (a) temperature, and (b) pressure.

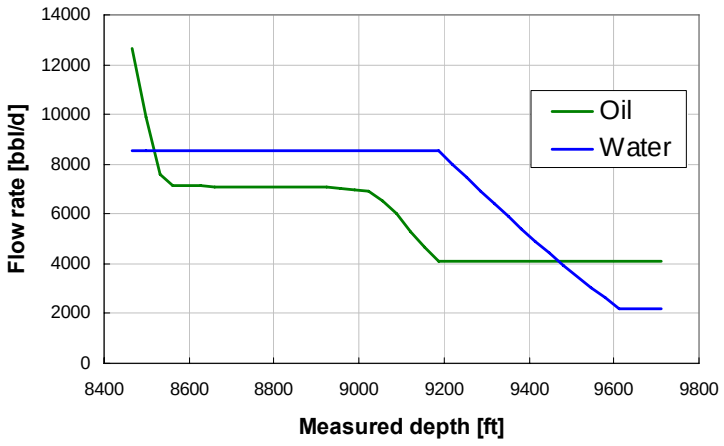

Fig. 26 Inverted flow rates.

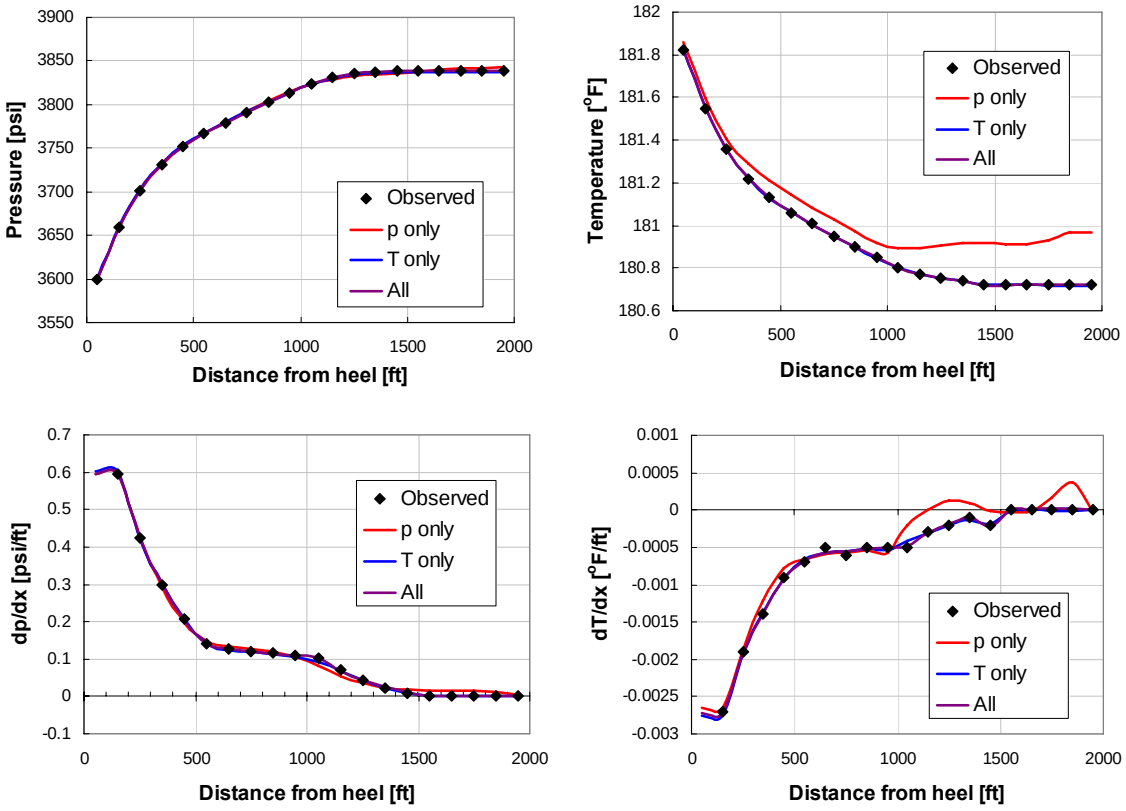

Fig.B.1 Observation and matched curves with different input data (Case A, oil).

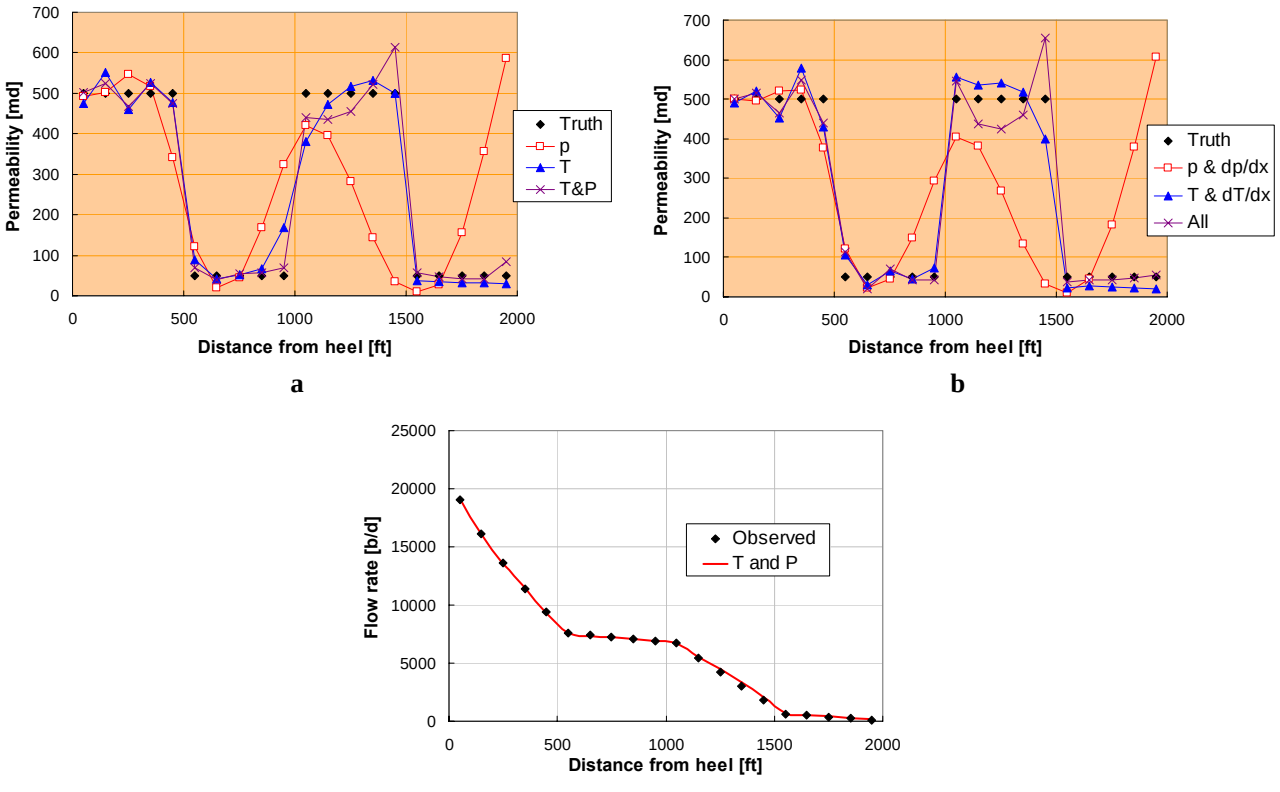

Fig. B.2 Inverted results for oil production case A, (a) permeability distributions from original data, (b) permeability distributions from derivative of the data, and (c) flow rate profile from temperature and pressure.

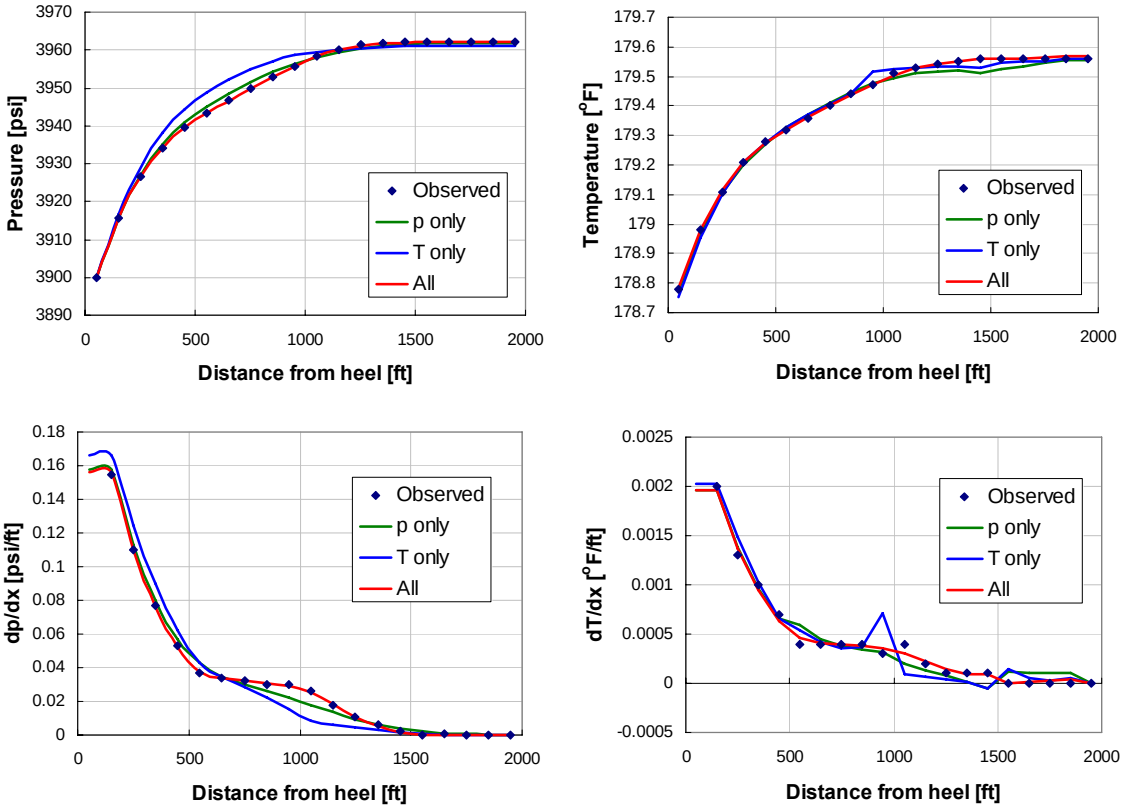

Fig.B.3 Observation and matched curves with different input data (Case A, gas).

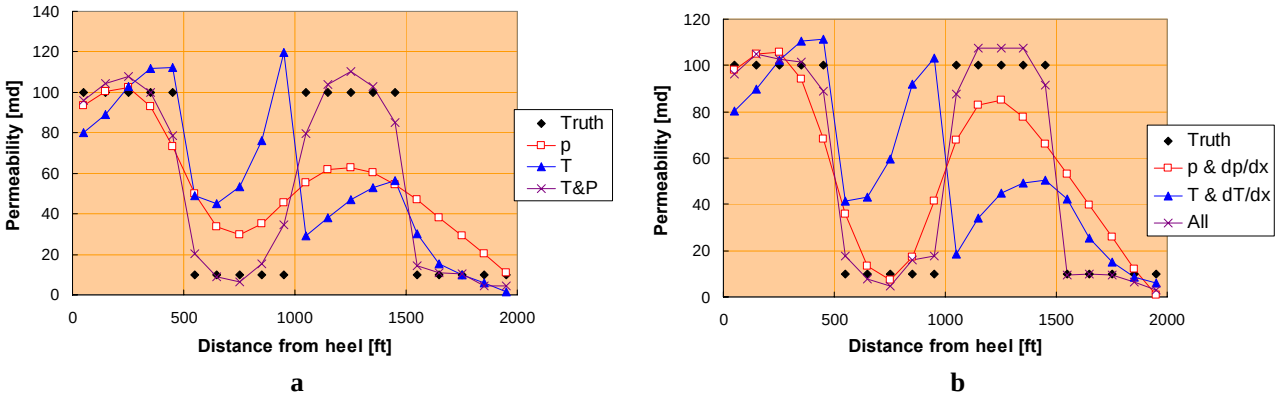

a b

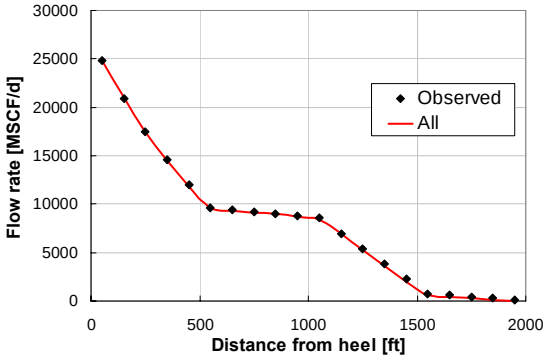

c

Fig. B.4 Inverted results for gas production case A: (a) permeability distributions from original data, (b) permeability distributions from derivative of the data, and (c) flow rate profile from all input data.

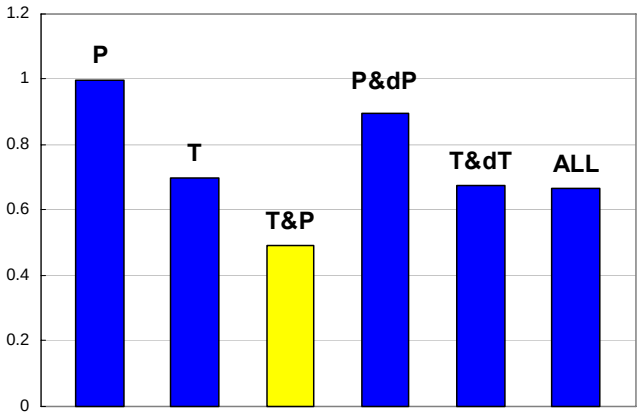

Fig. B.5 Average of normalized errors.